

Stress chatter on a fracture network reactivated by hydraulic fracturing

Andrés Felipe Peña Castro¹, Marco P Roth², Alessandro Verdecchia¹, John Onwuemeka¹, Yajing Liu¹, Rebecca M. Harrington², Yong Zhang³, and Honn Kao⁴

¹McGill University

²Ruhr University Bochum

³Peking University

⁴Geological Survey of Canada

November 24, 2022

Abstract

Source processes of injection induced earthquakes involve complex fluid-rock interaction often elusive to regional seismic monitoring. Here we combine observations from a local seismograph array in the Montney basin, northeast British Columbia, and stress modeling to examine the spatial and temporal evolution of the 30 November 2018 M 4.5 hydraulic fracturing induced earthquake sequence. The mainshock occurred at ~ 4.5 km in the crystalline basement two days following injection at ~ 2.5 km, suggesting direct triggering by rapid fluid pressure increase via a high-permeability conduit. Most of the aftershocks are located in the top 2 km sedimentary layers, with focal mechanisms indicating discrete slip along sub-vertical surfaces in a ~ 1 km wide deformation zone. Aftershock distribution is also consistent with static stress triggering from the M 4.5 coseismic slip. Our analysis suggests complex hydraulic and stress transfer between fracture/fault networks needs to be considered in induced seismic hazard assessment.

Stress chatter on a fracture network reactivated by hydraulic fracturing

A. F. Peña-Castro^{1,†}, M. P. Roth^{2,†}, A. Verdecchia¹, J. Onwuemeka¹, Y. Liu¹,
R. M. Harrington², Y. Zhang³, H. Kao⁴

¹Department of Earth and Planetary Sciences, McGill University, Montréal, Québec, Canada

²Institute of Geology, Mineralogy and Geophysics, Ruhr University Bochum, Bochum, Germany

³School of Earth and Space Sciences, Peking University, China

⁴Pacific Geoscience Centre, Geological Survey of Canada, Sidney, British Columbia, Canada

[†]These authors contributed equally to this work.

Key Points:

- Source parameter inversion and numerical modeling is performed for an M4.5 hydraulic fracturing induced earthquake sequence in northeast BC
- Mainshock is triggered by rapid fluid pressure increase via a hydraulic conduit channeling fluids from injection points to a basement fault
- Most aftershocks are triggered by a static Coulomb stress change resulting from mainshock coseismic slip

Corresponding author: Yajing Liu, yajing.liu@mcgill.ca

Abstract

Source processes of injection induced earthquakes involve complex fluid-rock interaction often elusive to regional seismic monitoring. Here we combine observations from a local seismograph array in the Montney Basin, northeast British Columbia, and stress modeling to examine the spatial and temporal evolution of the 30 November 2018 M_L 4.5 hydraulic fracturing induced earthquake sequence. The mainshock occurred at ~ 4.5 km in the crystalline basement two days following injection at ~ 2.5 km, suggesting direct triggering by rapid fluid pressure increase via a high-permeability conduit. Most of the aftershocks are located in the top 2 km sedimentary layers, with focal mechanisms indicating discrete slip along sub-vertical surfaces in a ~ 1 km wide deformation zone. Aftershock distribution is also consistent with static stress triggering from the M_L 4.5 coseismic slip. Our analysis suggests complex hydraulic and stress transfer between fracture/fault networks needs to be considered in induced seismic hazard assessment.

Plain Language Summary

Seismicity linked to hydraulic fracturing (HF) in shale gas exploration in western Canada has increased drastically over the last decade. However, details of induced seismicity sequence evolution and triggering mechanism(s) remain unclear. In this study, we integrate local seismic monitoring and numerical stress modeling for a M_L 4.5 HF induced earthquake sequence in northeast British Columbia, Canada, to reveal a two-step stress transfer process. A nascent, near-vertical fracture network in the sedimentary layers likely developed in the fault growth and basin infill of the Dawson Creek Graben Complex, and hydraulically channeled injected fluids to a thrust fault in the basement, leading to a rapidly increased fluid pressure that initiated the M_L 4.5 mainshock rupture. Static Coulomb stress change from the coseismic slip subsequently triggered the aftershocks along sub-parallel slip surfaces within the overlying sedimentary sequences. Our results also suggest the relative injection volumes and/or wellbore pressures required to create HF at each stage of neighboring wells may be diagnostic of presence of hydraulic connectivity to the basement, which tends to promote larger magnitudes of events.

1 Introduction

Seismicity related to fluid injection in the extraction of unconventional oil and gas resources has increased dramatically in North America in the last decade. While mod-

48 erate magnitude (M4+) earthquakes in the central and eastern US have been largely at-
49 tributed to continuous, large-volume wastewater disposal (Ellsworth, 2013), increasing
50 evidence suggests that high-pressure stimulation during hydraulic fracturing is linked to
51 a majority of M3+ earthquakes in the Western Canadian Sedimentary Basin (WCSB)
52 (Atkinson et al., 2016), including several M4+ events in 2015-2019 (Mahani et al., 2017,
53 2019), posing critical questions as to the triggering mechanisms, seismic hazard assess-
54 ment and regulatory policies in affected areas. Most of the WCSB M4 earthquakes are
55 inferred to have occurred on pre-existing, unmapped faults in the crystalline basement
56 (Bao & Eaton, 2016; Mahani et al., 2017), yet the stress state of the reactivated faults
57 and their hydraulic connectivity to the injection source region is largely unknown. Re-
58 mote dynamic triggering studies (Wang et al., 2015) have found evidence of direct and
59 delayed triggering of microseismicity near WCSB injection sites by perturbations of \sim
60 10 kPa, indicating critically stressed local receiver faults. On the other hand, static stress
61 drop estimates of induced events in WCSB suggest a wide range of values between \sim 0.1
62 and 100 MPa (Clerc et al., 2016; Zhang et al., 2016; Yu et al., 2019), suggesting a mix-
63 ture of local stress states, typical of their tectonic counterparts.

64 Triggering mechanisms proposed to explain the relation between fluid injection and
65 seismicity increase in WCSB mainly involve direct pore pressure increase as fluids mi-
66 grate in the medium (Bao & Eaton, 2016), or solid matrix stress changes to explain rapid
67 seismic response at distant locations (Deng et al., 2016), or a combination of the two (Yu
68 et al., 2019). However, on a regional scale, only \sim 0.3% of the \sim 12,000 HF wells ex-
69 amined in WCSB (1985-2015) were associated with M3+ earthquakes (Atkinson et al.,
70 2016). On a local scale, some HF wells with relatively larger injection volumes have in-
71 duced little to no seismicity, whereas significant M4+ events are mainly attributed to
72 wells of moderate injection volumes (Atkinson et al., 2016). These facts raise questions
73 as to how seismic propensity is influenced by local conditions, such as effective hydraulic
74 communication between the injection zones and nearby faults, and the composition and
75 stress state of pre-existing structures. We attempt to address the above questions in this
76 study by combining (1) a source parameter inversion of an M 4.5 HF induced seismic
77 sequence recorded by a local, dense seismograph array and (2) numerical modeling of stress
78 transfer informed by the injection time series.

79 The gas-bearing Montney Play extends from central Alberta to northeast British
80 Columbia (BC), where conventional oil and gas exploration in the sandstone and dolo-

81 stone reservoirs has been operating for decades near the foreland limit of the Late Cretaceous-
82 Paleocene Rocky Mountain thrust belt (Figure 1). Located between Fort St. John and
83 Dawson Creek in southern Montney, the Dawson Creek-Septimus area has witnessed a
84 drastic increase in seismicity, from no earthquakes reported by Natural Resources Canada
85 (NRCan) prior to 2013, to a total of ~ 205 cataloged events from 2013-2019 (Fig. S1).
86 With the overarching goal of monitoring seismicity and studying earthquake source pro-
87 cesses related to fluid injection in southern Montney, starting in July 2017, McGill Uni-
88 versity, Geological Survey of Canada (GSC), and BC Oil and Gas Commission (BCOGC)
89 jointly deployed a local dense array consisting of 15 broadband seismic stations in the
90 Dawson Creek-Septimus area (Figure 1). Additional 6 broadband stations were deployed
91 by the Ruhr University Bochum in 2019.

92 On 30 November 2018 (29 November 2018, local time), a M_L 4.5 earthquake oc-
93 curred ~ 25 km southeast of Fort St John, northeast BC, the second largest in the Mont-
94 ney Play related to hydraulic fracturing (Mahani et al., 2017). The mainshock was fol-
95 lowed by two significant aftershocks of M_L 4.2 and 3.4, leading to the BCOGC’s deci-
96 sion to maintain the suspension order of hydraulic fracturing activities at the well pad
97 linked to these events. To our knowledge, this is the first time a complete sequence of
98 a HF induced M_L 4.5 event was captured by a local dense seismograph array, which en-
99 ables us to determine event source parameters at an unprecedented resolution. Combined
100 with poroelastic stress models informed by injection history at the causal wells, our re-
101 sults reveal a sequential stress transfer process via both fluid-earthquake and earthquake-
102 earthquake interactions, during which the basement fault was reactivated by fluid flow,
103 and possibly aseismic slip along a nascent fracture network in the Dawson Creek graben
104 complex.

105 **2 Earthquake source parameter inversion**

106 **2.1 Data and methods**

107 We use waveform data collected at 100Hz at 15 broadband seismic stations, MG01-
108 09 (IRIS network code XL), MONT1-3, MONT6 (network code 1E), and NBC4, NBC7
109 (network code CN), to invert source parameters of the 30 November 2018 earthquake
110 sequence. Well locations and injection data are reported in the BCOGC database (<https://www.bcogc.ca/>,
111 last accessed 30 September 2019). A hybrid 1D velocity model (Table S1), where lay-

112 ers above 1 km are from Crust1.0 (Laske et al., 2013) and the deeper layers from (Mahani
113 et al., 2017) is applied in the following data analyses.

114 For a 20-day period centered at the 30 November 2018 M_L 4.5 mainshock (20 Novem-
115 ber 2018 to 10 December 2018), an automated Short-Time-Average/Long-Time-Average
116 (STA/LTA) detection employing *SeisComp3* (<https://www.seiscomp3.org/>) and the *Non-*
117 *LinLoc* location algorithm (Lomax et al., 2000) identified 18 events with M_L 0.8-4.5 (Sup-
118 plementary Materials). This STA/LTA catalog is further enhanced using a Multi-station
119 Matched-Filter (MMF) method (Chamberlain et al., 2018), which identifies additional
120 events by cross-correlating template waveforms with continuous three-component wave-
121 forms at all available stations. Our MMF search with 5 template events (Table S2), in-
122 cluding the M_L 4.5 mainshock and its two largest aftershocks, yields a total of 302 events
123 in the 20-day period; 203 detections have at least 4 phase picks for an initial location es-
124 timate (Figure 1), with average horizontal/vertical initial *NonLinLoc* location errors of
125 6.7/4.6 km.

126 We use two relocation algorithms, *HypoDD* (Waldhauser & Ellsworth, 2000) and
127 *GrowClust* (Trugman & Shearer, 2017), to better constrain the hypocenters of the 203
128 MMF detections. *HypoDD* results in a total of 68 relocated events and relative horizon-
129 tal and vertical location errors of 60 and 80 m, respectively. *GrowClust* relocated 59 events,
130 with location errors of 520 m (horizontal) and 450 m (vertical). Both algorithms yield
131 similar relocated hypocenters (Figure 3 and Figure S3). As the travel time residuals are
132 nominally smaller and number of relocated events is slightly larger with *HypoDD* (Fig-
133 ure S4), we will present event locations from this method in the following sections. We
134 use the probabilistic earthquake source inversion framework *Grond* (Heimann et al., 2018)
135 to compute full moment tensors, including non-double couple components, of one fore-
136 shock, the M_L 4.5 mainshock, and three aftershocks as listed in Tables S4 and S5. The
137 seismic moment, corner frequency, and static stress drop values of the mainshock and
138 the largest aftershocks are estimated using spectral fitting and used in estimating the
139 radius of the coseismic rupture in Section 3.2. See Supplementary Materials for details
140 of parameter choices in the source parameter analysis. Due to the small magnitudes of
141 most events in the sequence, further improvement in source parameter inversion would
142 require an even denser station coverage near the epicentral area and a high resolution
143 local 3D velocity model.

144 2.2 Cataloged seismicity and relation to fluid injection

145 Nearly all the STA/LTA cataloged seismicity in 2018 was spatially correlated with
 146 injection well pads, with most intense activity clustered near stations MONT1, MG01,
 147 MG03, MG05, and the epicentral area of the M_L 4.5 sequence (Figure 1). However, based
 148 on the 2018 seismicity and well distribution, there is no obvious correlation between cu-
 149 mulative injection volume and the number of induced earthquakes or their maximum mag-
 150 nitude. For example, the well located ~ 10 km northeast of MG09 had a total injection
 151 volume of 2.5×10^5 m³ with negligible seismicity detected within a ~ 5 km radius, whereas
 152 the two horizontal wells that were stimulated within 15 km of the M_L 4.5 epicenter had
 153 only finished a total of 13 ($\sim 1.4 \times 10^4$ m³ injected volume) of the 50-60 planned stages
 154 before the M_L 4.5 occurred.

155 The initial locations of the MMF detected events of the 30 November 2018 sequence
 156 highlight a primarily northwest-southeast trending structure, which is consistent with
 157 the seismicity trend illustrated by the NRCan reported events in this area from 2013-
 158 2019 (Fig. S1). Furthermore, the focal mechanism solution of the M_L 4.5 mainshock il-
 159 lustrates a NW-trending focal plane, similar to the August 2015 M_w 4.6 HF induced earth-
 160 quake ~ 120 km northwest of Fort St. John (Mahani et al., 2017). The thrust-faulting
 161 mechanism of both $M_{4.5+}$ earthquakes suggest that they occurred on pre-existing faults
 162 that are optimally oriented in the NE-SW trending maximum regional horizontal stress
 163 direction (S_{Hmax}) (Heidbach et al., 2018) (Figure 1).

164 Figure 2 illustrates the temporal relation between MMF detected seismicity and
 165 the per-stage injection volume along two horizontal wells (HW1 and HW2) actively stim-
 166 ulated prior to the M_L 4.5 sequence. Of the 302 detections, 32 occurred prior to the first
 167 stage of HW1, with the largest being an M_L of 1.36; 41 occurred during the combined
 168 13 stages (the last stage ended 12 minutes before the origin time of the M_L 4.5 main-
 169 shock) with the largest being an M_L of 2.11; 147 occurred in the 48 hours following the
 170 mainshock, and 82 occurred in the subsequent days (until 10 December 2018). Most of
 171 the seismic moment was released within one hour by the mainshock and two largest af-
 172 tershocks. The cumulative injection volume of the 13 completed stages is $\sim 1.4 \times 10^4$
 173 m³, an order of magnitude lower than that predicted by the inferred linear relationship
 174 between the maximum magnitude and total injection volume (McGarr, 2014). The per-
 175 sistent deviation from the injection volume-maximum magnitude relation reported for

176 several HF induced M4+ earthquakes in the WCSB (Atkinson et al., 2016) suggests that
177 they may have distinct source mechanisms from those induced by wastewater disposal
178 and enhanced geothermal stimulation.

179 **2.3 Relocated seismicity and inferred fracture network**

180 Figure 3 shows that most of the relocated events cluster around the terminus of
181 the horizontal wells, demonstrating a clear spatial coincidence to the stages stimulated
182 prior to the mainshock. The clear spatiotemporal proximity between injection and seis-
183 micity (Figures 2 and 3) indicates that stimulation at HW1 and HW2 are most likely
184 the direct cause of this M_L 4.5 sequence. The fault plane solutions of the M_L 4.5 main-
185 shock and its three largest aftershocks (M_L 4.2, 3.6 and 2.8) exhibit a mix of thrust and
186 strike-slip kinematics, suggesting both types of reactivated slip surfaces are approximately
187 optimally oriented in the regional stress field, and that the two least compressive stresses
188 of the local ambient stress field may be close in magnitude.

189 Except for the M_L 4.5 mainshock and a few other events relocated in the crystalline
190 basement, nearly all relocated earthquakes are in the upper ~ 2.5 km of sedimentary lay-
191 ers above the horizontal wells drilled through the Lower Montney formation, and exhibit
192 a sub-vertical distribution (Figure 3c and 3d). We interpret the near-vertical structure
193 defined by relocated seismicity and primarily strike-slip fault plane solutions of three largest
194 aftershocks as a nascent fault zone in which deformation has yet to accumulate to cre-
195 ate a through-going planar slip surface. The width of the deformation zone is ~ 1 km
196 as suggested by hypocenters with *HypoDD* horizontal/vertical relocation errors of 60/80
197 m. Such a relatively immature fault zone may evolve through the linkage of distributed
198 deformation bands as deformation progresses, similar to fault zone growth documented
199 in sedimentary rocks in Utah (Shipton & Cowie, 2001). Although the seismicity distri-
200 bution suggests a limited fault interaction between the basement fault on which the M_L
201 4.5 mainshock occurred and the presumed fault network in the overlying sedimentary
202 layers, their spatial clustering and temporal correlation with the injection time history
203 at HW1 and HW2 indicates an effective stress transfer process between the two fault sys-
204 tems.

3 Numerical modeling of stress transfer

3.1 Poroelastic stress model

As the mainshock occurred within two days from the onset of injection, but at a distance of over 2 km from the injection depth, we hypothesize that a highly permeable conduit may have facilitated fluid transport from the injection sources to the mainshock fault, hence rapidly increased the pore pressure on the fault within 1-2 days, which was sufficient to trigger the mainshock. To test the hypothesis, we develop a poroelastic stress model using the finite element software *Comsol Multiphysics*[®] following a linear poroelasticity framework (Biot, 1941). Two high-permeability zones are embedded in the model domain: a vertical conduit allowing fast fluid migration from the injection depth to the basement, and a damage zone flanking the mainshock fault plane, with orientation inferred from its focal mechanism solution (Figure 3b). See Supplemental Materials for model parameter details. Using the injection time series along HW1 and HW2 (Figure 2) and assuming a permeability contrast of 10^{-12} m² within the conduit zones and 10^{-16} - 10^{-19} m² within the country rock, pore pressure at the mainshock hypocenter effectively increases by ~ 0.1 MPa, which is ~ 1 -2 orders of magnitude higher than the stress perturbations associated with dynamic triggering of seismicity in WCSB (Wang et al., 2015, 2019). Without such high-permeability conduits, inferred pore pressure and poroelastic shear/normal stress changes on the mainshock fault are negligible in amplitude (1.5×10^{-4} MPa) within two days of injection onset (Figure S8). Such stress perturbations are significantly lower than previously observed dynamic triggering thresholds (Wang et al., 2015, 2019), rendering the physical model with conduits as being more plausible.

3.2 Coulomb stress model

Next, we use *Coulomb 3.3* (Toda et al., 2011) to calculate the Coulomb stress change $\Delta CFS = \Delta\tau - \mu(\Delta\sigma + \Delta p)$ due to the coseismic slip from the mainshock, resolved onto a receiver fault plane following the kinematics (strike, slip, rake) of the largest aftershock (M_L 4.2) (Table S4). Here, $\Delta\tau$ is the change in shear stress (positive in the direction of the receiver fault slip), μ is the friction coefficient, $\Delta\sigma$ is the change in normal stress (positive when the receiver fault is unclamped), and Δp is the pore pressure change. We assume the coseismic slip is uniformly distributed on a circular crack with a radius constrained by the mainshock corner frequency estimate and the seismic mo-

236 ment estimated from the moment tensor solution (Supplementary Materials, Figures S5-
237 S7). As shown in Figures 3c and 3d, except for a single event that does not cluster around
238 the stimulated stages, all the relocated aftershocks are distributed within the positive
239 Coulomb stress regime, strongly suggesting the continuation of the sequence by earthquake-
240 earthquake interaction via static Coulomb stress triggering. We also conduct a finite slip
241 inversion of the M_L 4.5 mainshock using all the 15 stations (Supplementary Materials).
242 Despite the more heterogeneous slip distribution over a broader area and hence smaller
243 amplitudes of Coulomb stress changes, nearly all aftershocks are still located within the
244 positive Coulomb stress regime (Figure S10).

245 4 Discussion

246 4.1 Two-step stress transfer

247 The relative offset between the injection depth and the M_L 4.5 hypocenter suggests
248 that while the initial stress perturbation to induce larger magnitude earthquakes may
249 have resulted from injection activity, the interaction between natural fault systems in
250 the basement and the overlying sedimentary layers dictates the seismicity evolution. The
251 focal mechanism solution of the mainshock suggests that its orientation in the regional
252 stress field is optimal for reactivation, thus, the long term deformation history may have
253 simply been time-advanced through the pressure perturbation from injection. The roughly
254 east-west trend of the nodal and fault planes depicted in Figures 3a and 3b are also con-
255 sistent with the general trend of the Dawson Creek Graben Complex, and the estimated
256 $\sim 50^\circ$ dip angle is consistent with a normal fault that has been reactivated in the present-
257 day ambient stress field (Barclay et al., 1990). The spatially diffuse distribution of af-
258 tershocks suggests a network of unconnected slip surfaces, such as those documented in
259 young (low cumulative offset) fault systems that form in porous sedimentary rocks (Shipton
260 & Cowie, 2001). Fault growth begins in such sedimentary rocks with short segments of
261 slip surfaces that eventually link up as deformation accumulates, where remaining un-
262 connected surfaces grow into a damage zone with continued deformation (Shipton & Cowie,
263 2001). The distribution of aftershocks directly above the mainshock fault would be a seis-
264 mic indicator of the presence of such a nascent fault system that likely formed during
265 synchronous basin infill with graben formation, and likely functioned as a high-permeability
266 pathway to funnel fluids to the mainshock fault. The separation between the mainshock
267 slip surface and the aftershock zone may suggest that the proposed graben fault and sub-

268 vertical fracture network do not yet have an intersecting slip surface. However, interact-
269 ing faults are not required to be geometrically or kinematically linked to transfer stress,
270 but rather, can interact through overlapping damage, or strain fields (Trudgill & Cartwright,
271 1994; Peacock et al., 2017).

272 Figure 4 provides a conceptual framework for the coeval formation of the subsur-
273 face structure consistent with the observations and numerical modeling results presented
274 here. As the initial tectonic regime during graben formation was extensional, sediment
275 infill began, and the progressive growth of the graben may have caused strain accumu-
276 lation along a zone of weakness in the overlying sediments, where a diffuse network of
277 slip surfaces formed as basin infill continued to accumulate (shown as the vertical col-
278 umn of black lines cutting through the dolostones and limestones in Figure 4). The old-
279 est dolostone and limestone sediments of the Debolt formation adjacent to the basement
280 would have experienced the most cumulative offset, and thus would be expected to have
281 the most extensively developed fracture network relative to the younger sedimentary lay-
282 ers deposited above (Barclay et al., 1990). Due to the low regional deformation rate (Kao
283 et al., 2018), the cumulative offset in the weak zone extending from the basement con-
284 tact to the surface would possibly be low enough to prevent a through-going slip surface
285 to form within. As cumulative offset should correlate with fracture network density, the
286 latter would also be expected to gradually decrease toward the surface to negligible val-
287 ues. The fracture network also correlates with permeability, which is also expected to
288 increase with the age of sediments, and hence better facilitate fluid transport at greater
289 depth (Caine et al., 1996). Once the mainshock is triggered by the fluids traveling from
290 the injection points to the basement fault, the fracture network provides a zone of weak-
291 ness susceptible to further triggering via the Coulomb stress perturbation from the static
292 offset of the mainshock. The Coulomb stress triggering mechanism would also be con-
293 sistent with the dearth of aftershocks observed in the stress shadow directly above the
294 mainshock (Figure 3d), where the negative Coulomb stress change could function to clamp
295 fractures closed directly outside the focal volume (in the dolostone and limestone layer).

296 The lack of seismicity in the dolostone and limestone layer could also be manifes-
297 tation of effective fault strengthening as fluids migrate downward through the fracture
298 network, where porosity development in the dolomitization process would favor strong
299 dilatancy, a mechanism that has been shown to inhibit dynamic deformation in landslides,
300 glacier tills, and fault gouges (Marone et al., 1990; Moore & Iverson, 2002), and leads

301 to aseismic slip in various tectonic settings (Segall et al., 2010; Liu, 2013). Stress load-
302 ing from aseismic creep has been proposed as an alternative mechanism for triggering
303 earthquakes under fluid injection (Bhattacharya & Viesca, 2019; Cappa et al., 2019), in
304 particular for events that occur at spatial and temporal scales unfavorable for fluid dif-
305 fusion or poroelastic stress triggering (Eyre et al., 2019). In our model, pore pressure in-
306 creases by 0.1 MPa on the mainshock fault within 2 days of injection onset when per-
307 meability in the near-vertical conduit is assumed to be 10^{-12} m²; a lower permeability
308 of 10^{-13} m² would result in a pore pressure increase of ~ 0.001 MPa for the same time
309 scale. Our proposed model is thus more compatible with a combined loading effect from
310 fluid diffusion and possible aseismic creep along the near-vertical fracture network.

311 The well treatment in the Upper Montney formation in May 2018 also induced a
312 similar number of events, compared with the November sequence (17 vs. 20), based on
313 our automated STA/LTA catalog, although the sequence in May had a maximum mag-
314 nitude of M_L 2.3 and there were no felt reports. While the fracture network depicted in
315 Figure 4 likely extends through the well bores used for the May 2018 treatment in the
316 Upper Montney formation, we infer that the hydraulic communication from the Upper
317 Montney to the basement fault must not have existed, otherwise the larger injection vol-
318 ume and longer injection period in May may have triggered M_L 4+ event(s) prior to the
319 treatment of the Lower Montney in November.

320 **4.2 Implications for seismic hazard and regulation**

321 The HF process requires building up downhole pressures to values roughly equal
322 to or greater than the magnitude of the least compressive stress (σ_3) in order to initi-
323 ate fractures. It has been hypothesized that the fracturing process may be less effective
324 for wells hydraulically connected to well developed, pre-existing basement fault systems
325 (Kozłowska et al., 2018), similar to the case suggested in our conceptual model (Figure
326 4). Fault conduit behavior, particularly in crystalline (basement) rocks, could funnel flu-
327 ids away from the volume of the target reservoir, and provide an explanation for cases
328 (Atkinson et al., 2016), including this study, where the inferred injection volume-maximum
329 magnitude relationship (McGarr, 2014) does not hold.

330 Multiple lines of evidence are in general consistent with the above reasoning. Based
331 on the per-stage injection volume reported by BCOGC, injection into the Lower Mont-

332 ney formation associated with the November 2018 M_L 4.5 required over twice volume
333 per stage of fluid for the HF process when compared with horizontal wells stimulated
334 directly above (~ 300 m) in the Upper Montney from the same vertical well pad in May
335 2018. The average injection volume required for the May treatment in the Upper Mont-
336 ney formation was 544 m^3 per stage compared with $1,190 \text{ m}^3$ per stage for HW1 and HW2
337 in the Lower Montney. If we assume that the pressure needed to overcome the regional
338 σ_3 is the same in the wells located in the two formations separated in depth only by 300
339 m, it implies that larger volumes of HF fluid were needed in comparable rock volumes
340 to achieve the same downhole pressure in the Lower Montney. The most plausible ex-
341 planation for the difference in the required fluid volume is that fluid is being lost while
342 or shortly after pumping activity attempts to drive pressure up, which is consistent the
343 conceptual model of the fracture network conduit (Figure 4) funneling fluids to the base-
344 ment fault via the two intersecting damage zones.

345 The fluid conduit model proposed here is also consistent with the relatively low,
346 $\sim 50\%$, flowback rate for WCSB HF wells reported by BCOGC and in Alberta (Bao
347 & Eaton, 2016), which implies that more than half of the injected fluids remain in the
348 subsurface and likely contribute to the sustained pressurization of existing fault zones
349 connected to fluid pathways. A similar spatial pattern of larger magnitude events oc-
350 ccurring in the basement while nearly all aftershocks in the sedimentary layers has been
351 observed at HF wells near the Crooked Lake, Alberta, where one of the wells associated
352 with an M_w 3.9 reported a flowback rate of merely $\sim 7\%$ (Bao & Eaton, 2016). Although
353 on a broad, regional scale HF injection volume has been shown to correlate with the fre-
354 quency of earthquakes in the Duvernay formation, Alberta (Schultz et al., 2018), obser-
355 vations presented in this study suggest a possible relation to the relative magnitude, if
356 examined across nearby wells. Industrial operators often have real-time information re-
357 garding relative volumes needed to reach overpressure levels at neighboring wells. If cer-
358 tain wells require higher volumes of fluids compared to nearby wells to reach overpres-
359 sure levels, it could serve as an effective diagnostic tool to identify possible presence of
360 faults hydraulically connected to the injection sources, and ultimately, help avoid induc-
361 ing large magnitude events.

5 Conclusions

In this study, we combined seismic observations and numerical stress modeling to investigate the source processes of an M_L 4.5 (30 November 2018) hydraulic fracturing (HF) induced earthquake sequence in the Dawson Creek-Septimus area of the Montney Basin, British Columbia. This event was the second largest HF induced earthquake in BC, and the first detected by a local dense seismic array. For a 20-day period centered at the mainshock origin time, we enhanced the automatic STA/LTA catalog by a multi-station matched-filter (MMF) method. The MMF catalog consists of a total of 302 detections, out of which 203 have initial location solutions and 68 were relocated. The M_L 4.5 mainshock occurred at a depth of ~ 4.5 km in the crystalline basement, about two days following the onset of injection at ~ 2.5 km along two nearby horizontal wells. The large spatial but short temporal separation between the onset of injection and the occurrence of the mainshock suggests direct triggering by rapid fluid pressure increase via a high-permeability conduit connecting the two sources, which we confirmed with poro-elastic stress modeling. The presence of such a hydraulic conduit is also supported by the much higher per stage injection volumes required to initiate HF in the Lower Montney than those in the Upper Montney layer ~ 300 m above.

Relocated aftershocks are mainly in the top 2 km sedimentary layers, with predominantly strike-slip focal mechanisms indicating discrete slip along sub-vertical surfaces in a ~ 1 km wide deformation zone. The deformation zone likely represents a nascent, near-vertical fracture network developed in the fault growth and basin infill of the Dawson Creek graben complex, and serves as a hydraulic conduit channeling fluids to the thrust fault in the basement, where the M_L 4.5 mainshock ruptured. Coulomb stress model suggests that most of the aftershocks were triggered by the static stress transfer from the M_L 4.5 coseismic slip. Our results also suggest that the relative injection volumes and/or well bore pressures at each HF stage of neighboring wells may be diagnostic of the presence of hydraulic connectivity to the crystalline basement, therefore a possible monitoring strategy for preventing large magnitude of events.

Acknowledgments

This study was supported by Natural Sciences and Engineering Research Council of Canada Strategic Grant STPGP/494141-2016, Deutsche Forschungsgemeinschaft Grant 428868223, and partially by an Natural Resources Canada (NRCan) Energy Innovation grant and

394 BC Oil and Gas Commission (BCOGC). We thank Stuart Venables and BCOGC staff
395 for coordinating field logistics and communication with partners. Field deployment trips
396 were led by Greg Langston (McGill) with contributions from NRCan, BCOGC and the
397 RUB. Waveform data used in this study is archived at IRIS under network codes XL,
398 1E and CN (e.g., <http://ds.iris.edu/gmap/XL>).

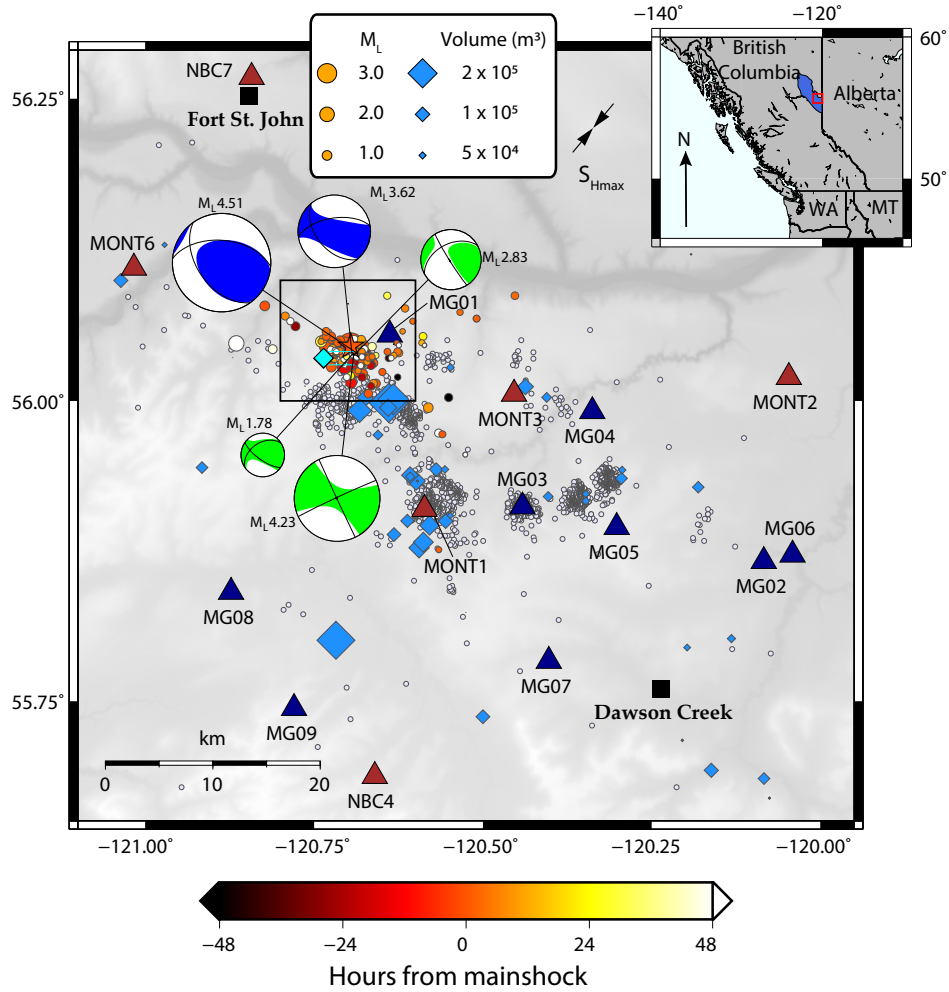


Figure 1. Earthquakes, seismic station, and hydraulic fracturing well distributions in the Dawson-Septimus area, northeast BC. Colored circles are MMF detected and located events 48 hours before and after the M_L 4.5 mainshock. MMF detections outside this period are colored in black (before) and white (after). Grey dots are STA/LTA detections January to December 2018. Blue diamonds are active HF wells in 2018 scaled by injection volume. Cyan diamond shows the well pad from which injection along two horizontal wells immediately preceded the M_L 4.5 event. S_{Hmax} represents regional maximum horizontal stress. The blue area in the inset shows the areal extension of the Montney Play in BC.

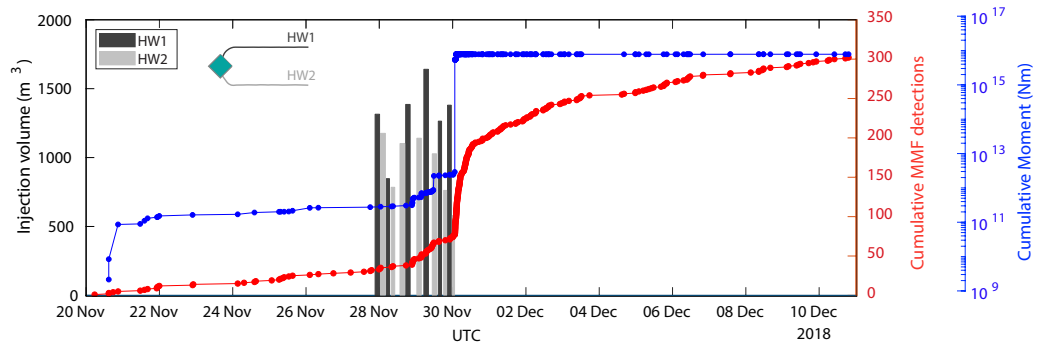


Figure 2. MMF-detected seismicity (red) and injection volume per stage (gray and black bars) along the two horizontal wells stimulated before the occurrence of the $M_L4.5$. No other wells were stimulated within 15 km of the epicenter during this period. Cumulative seismic moment shown in blue.

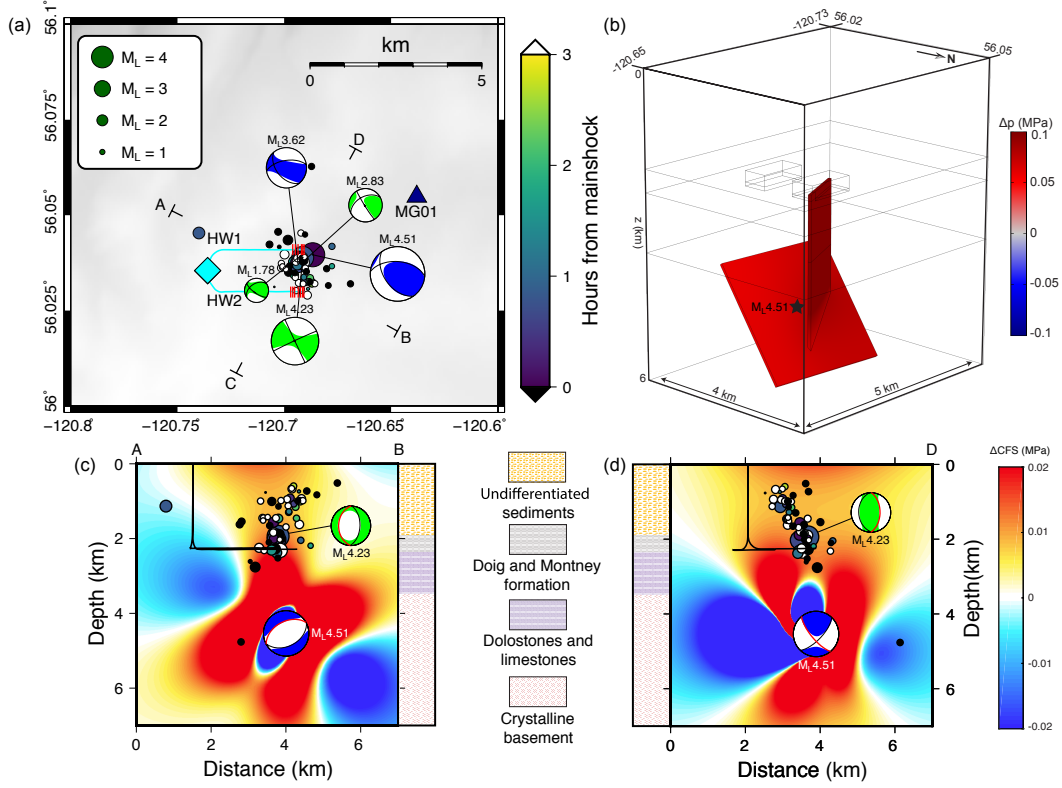


Figure 3. Relocated seismicity and Coulomb stress changes. (a) Map view of 68 earthquakes relocated with hypoDD, and focal mechanism solutions of the $M_L 4.5$ mainshock and four aftershocks. Red lines perpendicular to HF wells HW1 and HW2 trajectories depict the stages completed before the $M_L 4.5$. (b) Pore pressure change Δp due to injection history along HW1 and HW2 as in Fig. 2. Permeability of $k = 10^{-12} \text{m}^2$ is assumed along both the mainshock fault plane and a vertical conduit connecting the injection points to the mainshock fault. $k = 10^{-16}$ – 10^{-19}m^2 elsewhere in the model domain. See Methods for details. (c) and (d) Static Coulomb stress changes due to the coseismic slip of the mainshock, assuming a circular slip area under a static stress drop of 5.3 MPa (Methods and Supplement Information). Receiver fault kinematics (strike 245° , dip 88° , rake 0.4°) follow the focal mechanism solution of the largest ($M_L 4.2$) aftershock.

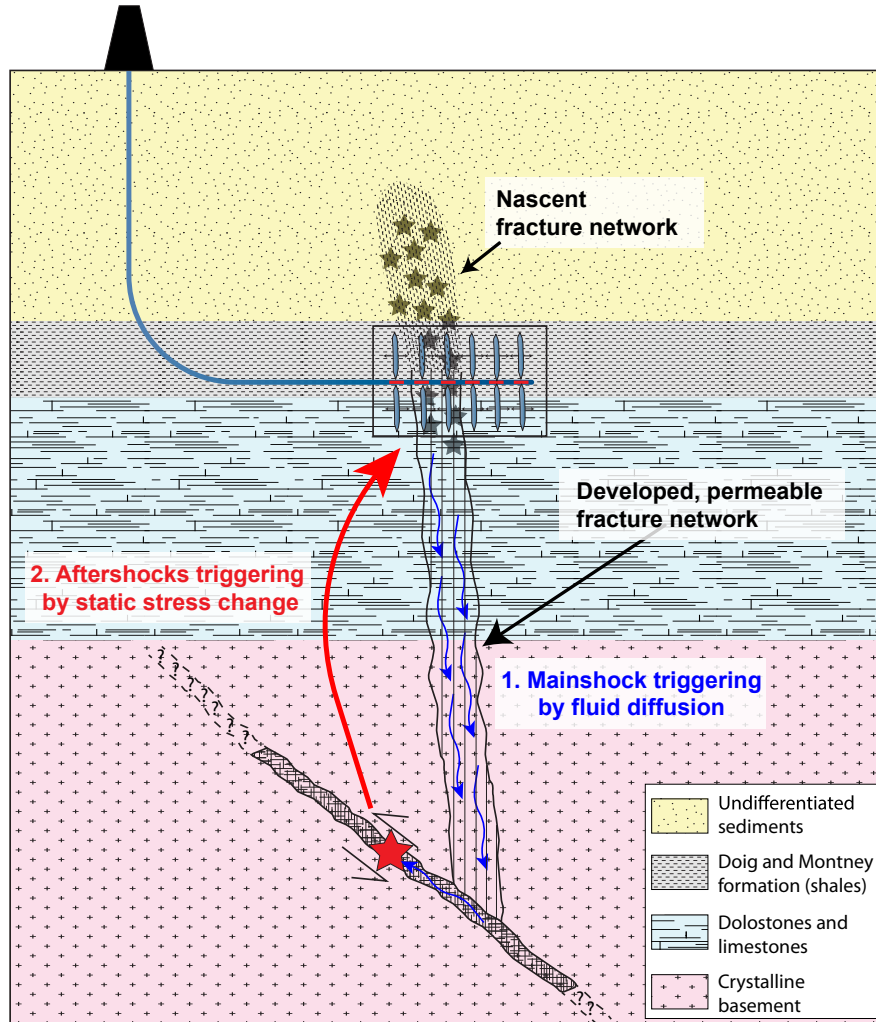


Figure 4. Conceptual diagram showing the two-step stress transfer during and shortly after HF stages. Injected fluid migrates (blue arrows) vertically through a developed, permeable fracture network to the basement fault and pore pressure increase triggers the mainshock (red star) fault plane. Static Coulumb stress changes due to the mainshock coseismic slip subsequently trigger aftershocks along a nascent fracture zone in the sedimentary layers.

References

- 399
- 400 Atkinson, G., Eaton, D. W., Ghofrani, H., Walker, D., Cheadle, B., Schultz, R., ...
- 401 Kao, H. (2016). Hydraulic fracturing and seismicity in the Western Canada
- 402 Sedimentary Basin. *Seismological Research Letters*, *87*, 631-647.
- 403 Bao, X., & Eaton, D. W. (2016). Fault activation by hydraulic fracturing in Western
- 404 Canada. *Science*, *354*, 1406–1409. doi: 10.1126/science.aag2583
- 405 Barclay, J., Krause, F., Campbell, R., & Utting, J. (1990). Dynamic casting and
- 406 growth faulting: Dawson Creek graben complex, Carboniferous-Permian Peace
- 407 River embayment, Western Canada. *Bulletin of Canadian Petroleum Geology*,
- 408 *38*(1), 115–145.
- 409 Bhattacharya, P., & Viesca, R. C. (2019). Fluid induced aseismic fault slip outpaces
- 410 pore fluid migration. *Science*, *364*.
- 411 Biot, M. (1941). General three-dimensional theory of poroelasticity. *J. Appl. Phys*,
- 412 *12*, 155–164.
- 413 Caine, J. S., Evans, J. P., & Forster, C. B. (1996). Fault zone architecture and per-
- 414 meability structure. *Geology*, *24*(11), 1025–1028.
- 415 Cappa, F., Scuderi, M. M., Collettini, C., Guglielmi, Y., & Avouac, J.-P. (2019).
- 416 Stabilization of fault slip by fluid injection in the laboratory and in situ. *Sci-*
- 417 *ence Advances*, *5*.
- 418 Chamberlain, C. J., Hopp, C. J., Boese, C. M., Warren-Smith, E., Chambers, D.,
- 419 Chu, S. X., ... Townend, J. (2018). EQcorrscan: Repeating and near-
- 420 repeating earthquake detection and analysis in Python. *Seismological Research*
- 421 *Letters*, *89*(1), 173–181.
- 422 Clerc, F., Harrington, R. M., & Liu, Y. (2016). Stress drop estimates and hypocen-
- 423 ter relocations of induced seismicity near Crooked Lake, Alberta. *Geophys.*
- 424 *Res. Lett.*, *43*, 6942–6951.
- 425 Deng, K., Liu, Y., & Harrington, R. M. (2016). Poroelastic stress triggering of the
- 426 December 2013 Crooked Lake, Alberta, induced seismicity sequence. *Geophys-*
- 427 *ical Research Letters*, *43*(16), 8482–8491.
- 428 Ellsworth, W. L. (2013). Injection-induced earthquakes. *Science*, *341*, 1225942-
- 429 1225942. doi: 10.1126/science.1225942
- 430 Eyre, T. S., Eaton, D. W., Garagash, D. I., Zecevic, M., Venieri, M., Weir, R., &
- 431 Lawton, D. C. (2019). The role of aseismic slip in hydraulic fracturing induced

- 432 seismicity. *Science Advances*, 5.
- 433 Heidbach, O., Rajabi, M., Cui, X., Fuchs, K., Müller, B., Reinecker, J., . . . Zoback,
434 M. (2018). The world stress map database release 2016: Crustal stress pattern
435 across scales. *Tectonophysics*, 744, 484 – 498. doi: [https://doi.org/10.1016/
436 j.tecto.2018.07.007](https://doi.org/10.1016/j.tecto.2018.07.007)
- 437 Heimann, S., Isken, M., Kühn, D., Sudhaus, H., Steinberg, A., Vasyura-Bathke, H.,
438 . . . Dahm, T. (2018). *Grond - A probabilistic earthquake source inversion
439 framework*. Retrieved 2018-08-27, from [http://pyrocko.org/grond/docs/
440 current/](http://pyrocko.org/grond/docs/current/) doi: 10.5880/GFZ.2.1.2018.003
- 441 Kao, H., Hyndman, R., Jiang, Y., Visser, R., Smith, B., Mahani, A. B., . . . He, J.
442 (2018). Induced seismicity in Western Canada linked to tectonic strain rate:
443 implications for regional seismic hazard. *Geophysical Research Letters*, 45,
444 11104-11115.
- 445 Kozłowska, M., Brudzinski, M. R., Friberg, P., Skoumal, R. J., Baxter, N. D., &
446 Currie, B. S. (2018). Maturity of nearby faults influences seismic hazard from
447 hydraulic fracturing. *Proceedings of the National Academy of Sciences*, 115(8),
448 E1720–E1729.
- 449 Laske, G., Masters, G., Ma, Z., & Pasyanos, M. (2013). Update on crust1. 0—a 1-
450 degree global model of earth’s crust. In *Geophys. res. abstr* (Vol. 15, p. 2658).
- 451 Liu, Y. J. (2013). Numerical simulations on megathrust rupture stabilized under
452 strong dilatancy strengthening in slow slip region. *Geophys. Res. Lett.*, 40,
453 1311–1316. doi: 10.1002/grl.50298
- 454 Lomax, A., Virieux, J., Volant, P., & Berge-Thierry, C. (2000). Probabilistic earth-
455 quake location in 3D and layered models. In *Advances in seismic event location*
456 (pp. 101–134). Springer.
- 457 Mahani, A. B., Kao, H., Atkinson, G. M., Assatourianas, K., Addo, K., & Liu, Y.
458 (2019). Ground motion characteristics of the 30 November 2018 injection
459 induced earthquake sequence in northeast British Columbia, Canada. *Seismo-
460 logical Research Letters*, 90(4), 1457-1467.
- 461 Mahani, A. B., Schultz, R., Kao, H., Walker, D., Johnson, J., & Salas, C. (2017).
462 Fluid injection and seismic activity in the Northern Montney Play, British
463 Columbia, Canada, with special reference to the 17 August 2015 Mw 4.6 in-
464 duced earthquake. *Bulletin of the Seismological Society of America*, 107(2),

- 465 542-552. doi: 10.1785/0120160175
- 466 Marone, C., Raleigh, C. B., & Scholz, C. H. (1990). Frictional behavior and con-
467 stitutive modeling of simulated fault gouge. *J. Geophys. Res.*, *95*(B5), 7007–
468 7025.
- 469 McGarr, A. (2014). Maximum magnitude earthquakes induced by fluid injection. *J.*
470 *Geophys. Res.*, *119*, 1008-1019. doi: 10.1002/2013JB010597
- 471 Moore, P. L., & Iverson, N. R. (2002). Slow episodic shear of granular materials reg-
472 ulated by dilatant strengthening. *Geology*, *30*, 843–846.
- 473 Peacock, D., Dimmen, V., Rotevatn, A., & Sanderson, D. (2017). A broader classifi-
474 cation of damage zones. *Journal of Structural Geology*, *102*, 179–192.
- 475 Schultz, R., Atkinson, G., Eaton, D. W., Gu, Y. J., & Kao, H. (2018). Hydraulic
476 fracturing volume is associated with induced earthquake productivity in the
477 Duvernay play. *Science*, *359*, 304–308. doi: 10.1126/science.aao0159
- 478 Segall, P., Rubin, A. M., Bradley, M., & Rice, J. R. (2010). Dilatant strengthening
479 as a mechanism for slow slip events. *J. Geophys. Res.*, *115*(B12305). doi: 10
480 .1029/2010JB007449
- 481 Shipton, Z. K., & Cowie, P. A. (2001). Damage zone and slip surface evolution over
482 μm to km scales in high-porosity Navajo sandstone, Utah. *Journal of Struc-*
483 *tural Geology*, *23*, 1825-1844.
- 484 Toda, S., Stein, R. S., Sevilgen, V., & Lin, J. (2011). *Coulomb 3.3 graphic-rich*
485 *deformation and stress-change software for earthquake, tectonic, and volcano*
486 *research and teaching-user guide* (Tech. Rep.). US Geological Survey.
- 487 Trudgill, B., & Cartwright, J. (1994). Relay-ramp forms and normal-fault linkages,
488 Canyonlands National Park, Utah. *Geological Society of America Bulletin*,
489 *106*(9), 1143–1157.
- 490 Trugman, D. T., & Shearer, P. M. (2017). Growclust: A hierarchical clustering
491 algorithm for relative earthquake relocation, with application to the Spanish
492 Springs and Sheldon, Nevada, earthquake sequences. *Seismological Research*
493 *Letters*, *88*(2A), 379–391.
- 494 Waldhauser, F., & Ellsworth, W. L. (2000). A double-difference earthquake location
495 algorithm: Method and application to the northern Hayward fault, California.
496 *Bulletin of the Seismological Society of America*, *90*(6), 1353–1368.
- 497 Wang, B., Harrington, R. M., Liu, Y., Kao, H., & Yu, H. (2019). Remote dynamic

- 498 triggering of earthquakes in three unconventional canadian hydrocarbon re-
499 gions based on a multiple-station matched-filter approach. *Bulletin of the*
500 *Seismological Society of America*, 109(1), 372–386.
- 501 Wang, B., Harrington, R. M., Liu, Y., Yu, H., Carey, A., & van der Elst, N. (2015).
502 Isolated cases of remote dynamic triggering in Canada detected using cat-
503 aloged earthquakes combined with a matched-filter approach. *Geophysical*
504 *Research Letters*, 42. doi: 10.1002/2015GL064377
- 505 Yu, H., Harrington, R., Liu, Y., & Wang, B. (2019). Induced seismicity driven by
506 fluid diffusion revealed by a near-field hydraulic stimulation monitoring array
507 in the Montney Basin, British Columbia. *Journal of Geophysical Research:*
508 *Solid Earth*, 124(5), 4694–4709.
- 509 Zhang, H., Eaton, D. W., Li, G., Liu, Y., & Harrington, R. M. (2016). Discrimi-
510 nating induced seismicity from natural earthquakes using moment tensors and
511 source spectra. *Journal of Geophysical Research: Solid Earth*, 121(2), 972-993.
512 doi: 10.1002/2015jb012603

Supporting Information for ”Stress chatter on a fracture network reactivated by hydraulic fracturing”

Andres F. Peña Castro^{1,†}, Marco P. Roth^{2,†}, Alessandro Verdecchia¹, John

Onwuemeka¹, Yajing Liu¹, Rebecca M. Harrington², Yong Zhang³, Honn

Kao⁴

¹Department of Earth and Planetary Sciences, McGill University, Montréal, Québec, Canada

²Institute of Geology, Mineralogy and Geophysics, Ruhr University Bochum, Bochum, Germany

³School of Earth and Space Sciences, Peking University, China

⁴Pacific Geoscience Centre, Geological Survey of Canada, Sidney, British Columbia, Canada

[†]These authors contributed equally to this work.

Contents of this file

1. Text S1 to S5
2. Figures S1 to S10
3. Tables S1 to S7

S1 Multi-station matched-filter detection

Each 6-second template waveform begins 0.1 s before the P-arrival and contains separate P- and S-wave phase recordings on three components. Table S2 lists the origin time and the number of secondary detections for each of the templates. Before performing the MMF detection by cross-correlation across all stations in a time step of 0.025 s, we re-sample the template waveforms to 40 sps and apply a bandpass filter of 2-10 Hz. Station NBC4 was not used in some cases due to multiple data gaps in the 20-day period. Detections are declared when the summed correlation function exceeds a pre-set threshold, empirically chosen to be 8 times the Median Absolute Deviation (MAD) of the day-long CC sum.

If at least one channel exhibits a CC value of at least 0.4 with respect to the template, a possible detection is declared. Detections for which an analyst observes visible P- and/or S-waves at the station for which the detection is generated are retained. We located detections that generate picks on at least four stations, and assume events with detections on fewer stations are co-located with templates.

S2 Seismicity relocation

Both approaches (*HypoDD* and *GrowClust*) use the reference *NonLinLoc* (Lomax et al., 2000) initial locations, differential travel times, and cross-correlation coefficients to simultaneously group and relocate events within similar clusters (Waldhauser & Ellsworth, 2000; Trugman & Shearer, 2017). We use slightly different settings for each approach. The *HypoDD* (Waldhauser & Ellsworth, 2000) relocation algorithm uses differential travel times from cross-correlation of event waveforms using 2.5 second time windows starting 1 sec prior to and 1.5 sec after the phase arrival pick, with waveforms bandpass filtered

between 2 and 15 Hz. We retain differential travel times between events with a cross-correlation coefficient of 0.6 or higher. Initial iterations weight the catalog phase picks relative to cross-correlation differential travel times by a ratio of 100:1 to constrain absolute hypocentral locations. The subsequent 20 iterations weight catalog phase picks to differential phase picks by a ratio of 1:100 to reduce the relative relocation error within the cluster. Following the relocation calculation, location error is then estimated by a bootstrap random replacement scheme with 100 trials. The above settings lead to a total number of 68 relocated events with relative horizontal and vertical location error of 60 and 80 m, respectively.

For the *GrowClust* (Trugman & Shearer, 2017) algorithm, we determine differential travel times using data cut by time windows starting 1.0 sec before and 1.5 sec after the P-arrival pick, and 1.0 sec before and 2.5 sec after the S-wave arrival pick. We apply a bandpass filter of 2-10 Hz prior to cross-correlation value calculation, and require a minimum of eight phases with cross-correlation coefficient values > 0.6 and an RMS cut-off of 0.3 s. The above parameter settings lead to 59 relocated events, with mean horizontal and vertical location error of 520 m and 450 m, respectively, a 10-fold reduction compared to the initial location errors. The relocations obtained with *GrowClust* are shown in Figure S3. Both relocation algorithms highlight similar features, where RMS travel-time residuals are lower for HypoDD than *GrowClust* (Figure S4).

S3 Earthquake source parameter estimation

We first estimate the station averaged M_0 and f_c values by fitting individual spectra using the Brune model (Brune, 1970) for events with signal to noise ratio $\text{SNR} > 2$ in the

frequency band of 0.1 - 45 Hz using magnitude dependent time windows (4 s for $M > 4$ events, and 2 s for $M < 4$ events) and a multi-taper spectral estimation (Prieto et al., 2007, 2009). The SNR is calculated using noise spectra estimated from time windows of identical length to the signal spectra. We first constrain the seismic moment (M_0) and spectral corner frequency values (f_c) using a least squares fit to the following equation (Brune, 1970; Boatwright, 1978):

$$\Omega(f) = \frac{\Omega_0 e^{-\left(\frac{\pi f t}{Q}\right)}}{\left(1 + \left(\frac{f}{f_c}\right)^{\gamma n}\right)^{1/\gamma}}, \quad (1)$$

where Ω_0 is the long-period spectra amplitude, Q is the seismic quality factor, t is the travel time, n is the spectral falloff rate, and γ is the corner shape determinant (e.g., (Abercrombie, 1995)). We then use the fitted Ω_0 and f_c values to determine values of moment and static stress drop ($\Delta\sigma$) for estimating average fault area and slip for the Coulomb stress calculation. The moment calculation is computed with

$$M_0 = \frac{4\pi\rho\beta^3\Omega_0 R}{U_{\phi\theta}}, \quad (2)$$

where ρ is the average crustal density (2.7 kg/m³), R is the hypocentral distance, β is the depth dependent shear wave velocity (Table S1), and $U_{\phi\theta}$ is the average radiation pattern for S-waves (Eshelby, 1957).

We can relate the static stress drop for a circular, two-dimensional fault to the scalar moment using the following equation (Burridge & Knopoff, 1964):

$$M_0 = \frac{16}{7}\Delta\sigma a^3 \quad (3)$$

where a is the fault radius. We then relate f_c to a using the following relationship (Madariaga, 1976):

$$a = \frac{0.32\beta}{f_c}. \quad (4)$$

Figures S5 and S6 show the spectra fitting of the mainshock and the stress drop spectra, respectively. Table S3 lists the corner frequency and stress drop values obtained through the fitting procedure described above.

We use the probabilistic earthquake source inversion framework *Grond* (Heimann et al., 2018) to compute full moment tensor solutions. We start by computing Greens Functions (GFs) with Qseis (Wang, 1999) over a $100 \times 100 \times 15$ km³ volume with step-length of 200 m using the velocity model in Table S1. We then cut event waveforms over 0.8-second time-windows starting 0.05 sec before the analyst-picked phase arrivals. The algorithm then simulates synthetic waveforms from a set of 18,000-30,000 trial models (centroid and moment tensors) within the GF volume and fits each synthetic waveform with the observed data for both P- and S-waves in both frequency and time domains, as well as waveform envelopes. The optimal moment tensor and centroid is determined based on a Bayesian bootstrap optimization, which enables full probabilistic bootstrapping of optimization solutions (Heimann et al., 2018). The bootstrapping optimization technique also provides an uncertainty estimation that typically decreases with increasing iterations.

Given that the source mechanism could potentially involve significant non-double couple components due to fluid injection and rupture on adjacent and/or intersecting fault structures, we estimate full moment tensor solutions (including isotropic, compensated-

linear vector dipole, and double couple components) to try and identify possible source complexity. We obtain robust moment tensor solutions for one foreshock, the mainshock, and 3 aftershocks (Tables S4 and S5). The focal mechanism and centroid solutions are consistent with the general trend of the relocated seismicity, and suggest a thrust fault solution for the mainshock, and predominantly strike-slip solutions for aftershocks in the sedimentary layers. Both types of solutions are consistent with roughly optimally oriented faults in the regional stress field. All estimated centroids lie within less than 300 m of their corresponding relocated hypocenters, and provide an independent validation of the hypocenter relocation.

S4 Poroelastic stress model The governing equations of linear poroelasticity can be written as (Wang & Kümpel, 2003):

$$G\nabla\nabla\mu + \frac{G}{1-2\nu}\nabla\epsilon - \alpha\Delta p = f(x, t) \quad (5)$$

$$\frac{1}{M}\frac{\partial p}{\partial t} + \alpha\frac{\partial\epsilon}{\partial t} - \nabla\cdot\left(\frac{\kappa}{\eta}\nabla p\right) = q(x, t) \quad (6)$$

where μ is the displacement vector, p is the excess pore pressure, $\epsilon = \nabla\cdot\mu$ is the volumetric strain, G is the shear modulus, ν is Poisson's ratio under drained conditions, α is the Biot coefficient, M is the Biot modulus, κ is the matrix permeability, η is dynamic viscosity of the fluid, f is the body force per unit volume acting on the solid matrix, and q is the fluid volume injection rate (fluid source density).

The stress-strain relation of the solid matrix when pore fluid p is under pressure is given by

$$\sigma_{ij} = \frac{2G\nu}{1-2\nu}\epsilon\delta_{ij} + 2G\epsilon_{ij} - \alpha p\delta_{ij} \quad (7)$$

where δ_{ij} is the Kronecker delta.

S5 Finite slip inversion

We invert the finite slip distribution of the M_L 4.5 mainshock, by assuming slip on either of the two conjugated fault planes from the mainshock focal mechanism solution (Table S4) (Zhang et al., 2012; Wang et al., 2017). The 4.2 km by 4.2 km fault plane is equally divided into $21 \times 21 = 421$ sub-faults (grid size 0.2 km) (Figure S10). The hypocenter is located at the center of the fault. Slip inversion uses the 1D velocity model as in Table S1. Velocity waveforms are integrated into displacement and band-pass filtered 0.05-1 Hz. Due to the small magnitude of the mainshock, we assume a maximum rupture velocity of 2.5 km/s and a rupture duration of 3 s for the inversion. Slip inversion results and corresponding Coulomb stress change are shown in Fig. S10. A higher resolution 3D velocity model and/or closer station-source distances would lead to a better constrained slip inversion for this relatively low magnitude event.

Figures

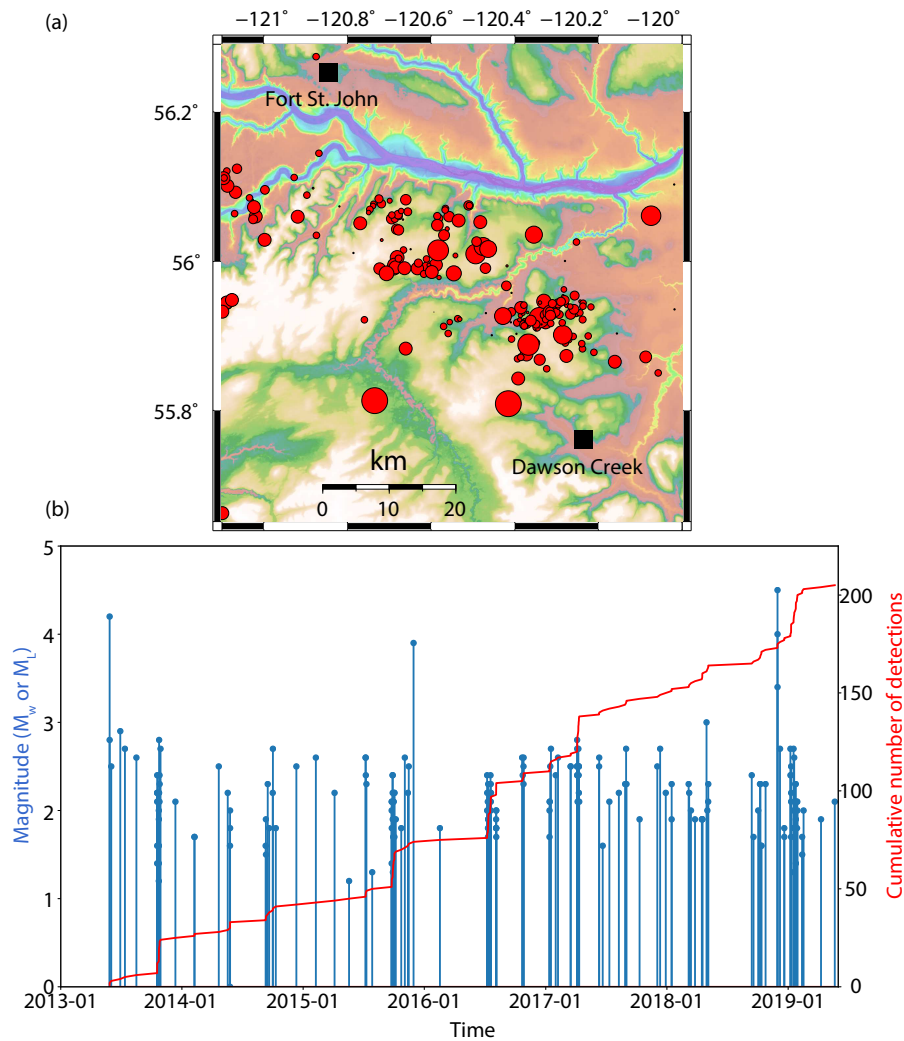


Figure S1. (a) Map overview of the seismicity reported by NRCan (*Natural Resources Canada Earthquakes Canada, GSC, Earthquake Search (On-line Bulletin)*, n.d.) from 2013 until June 2019 on the Dawson Septimus area. (b) Magnitude vs time (blue dots) of the same earthquakes shown in (a); red line indicates the cumulative number of earthquakes.

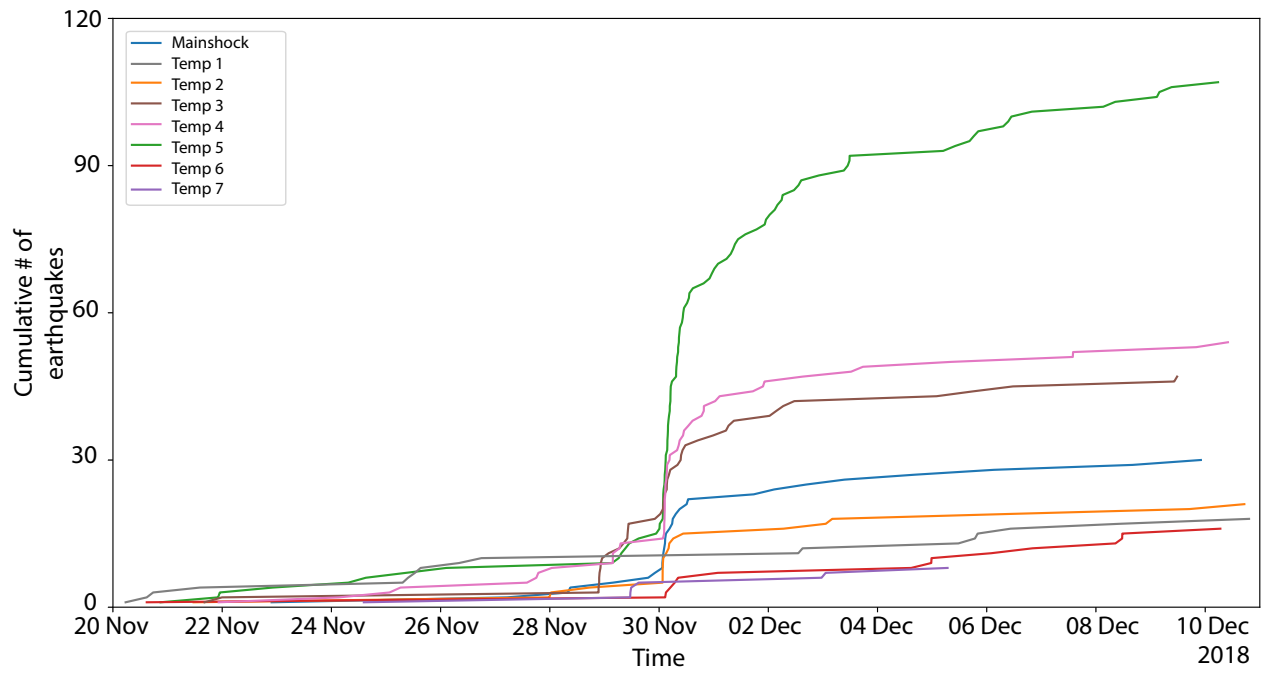


Figure S2. Number of earthquakes detected by each of the templates (Table S2) from Nov 20 until Dec 11. Templates 3 (brown line) and 4 (pink line) (the strongest aftershocks), and 5 detected a total of 178 more events than the Mainshock template (blue line).

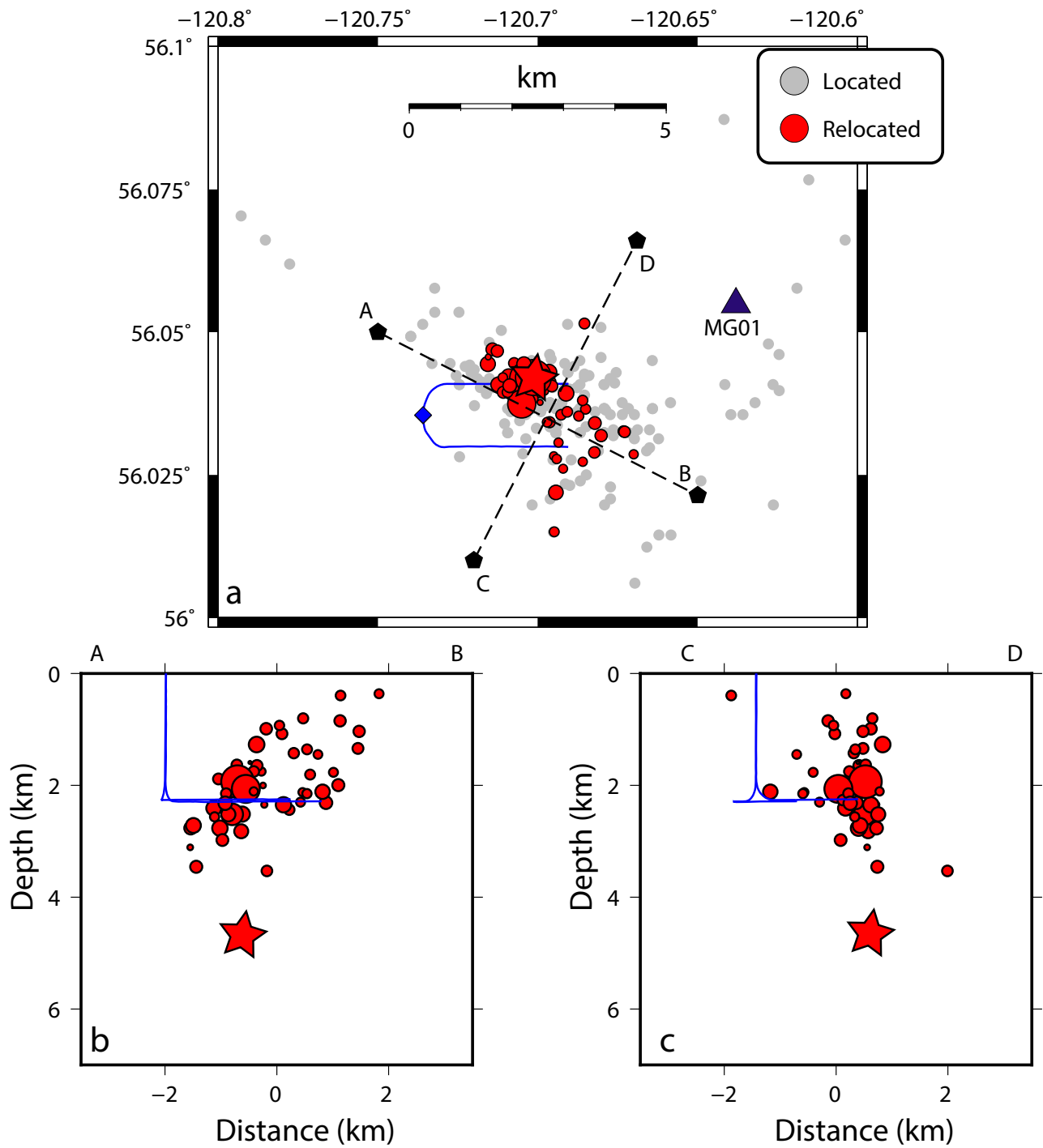


Figure S3. (a) Map view of earthquakes relocated using *GrowClust* (red circles) and initial locations determined with *NonLinLoc* (gray circles). (b) and (c) are relocated earthquake profiles (same as Figure 3)). Red star shows the Mainshock relocation.

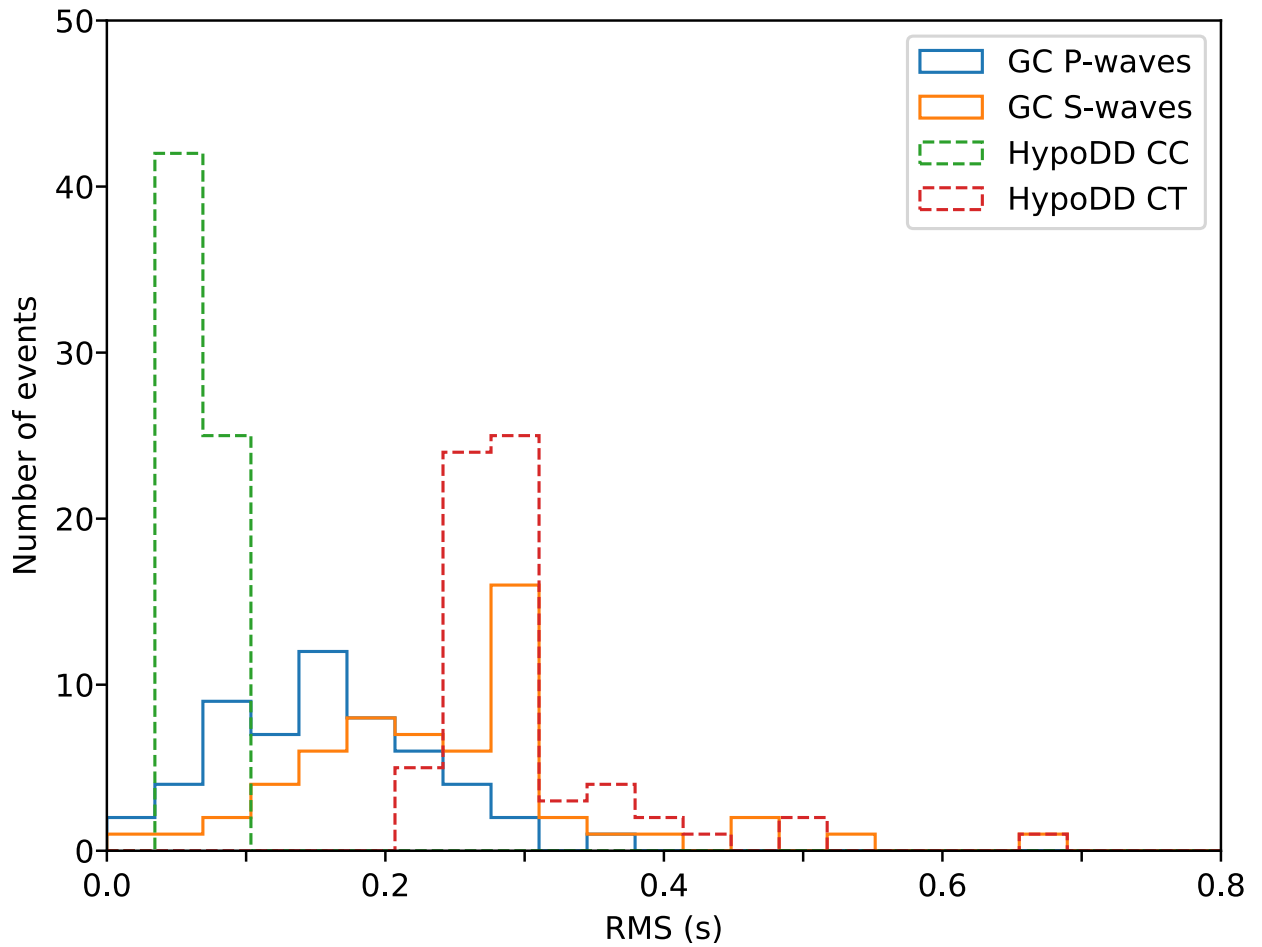


Figure S4. Root-Mean-Square (RMS) residual differential times for each of the relocation methods (*GrowClust* and *HypoDD*). *GrowClust* outputs RMS for P- and S- waves separately while *HypoDD* shows the RMS for the iteration of the catalogue (CT) and the cross-correlation procedure (CC). RMS relocation values are lower for *HypoDD* solutions, as indicated by the green dashed line.

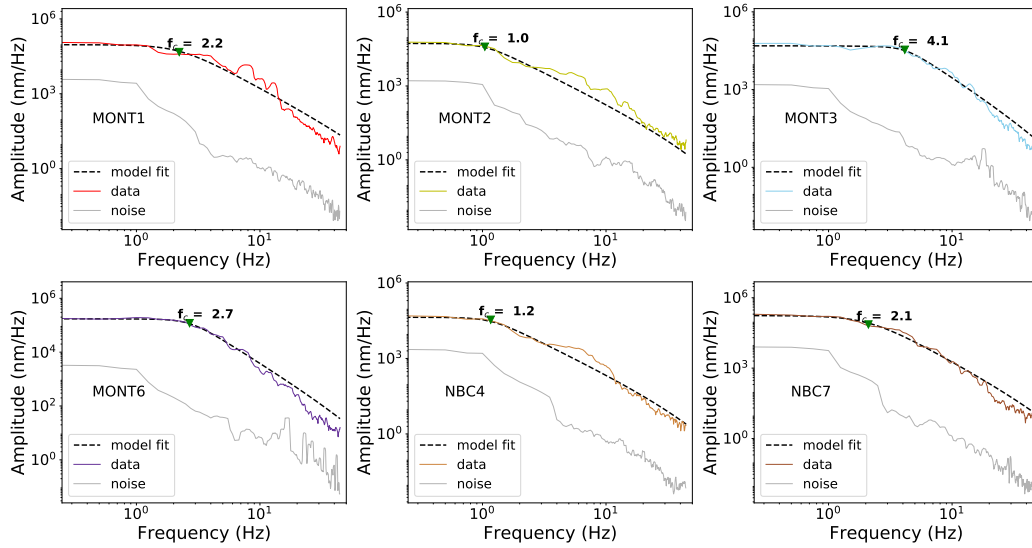


Figure S5. Single-spectrum fit of the windowed waveform data of the mainshock for various stations. Dotted-black and gray lines represent the model fit of the mainshock spectra (colored lines) and the noise spectra, respectively. Corner frequency estimates from each fit at an individual station are indicated by green triangles.

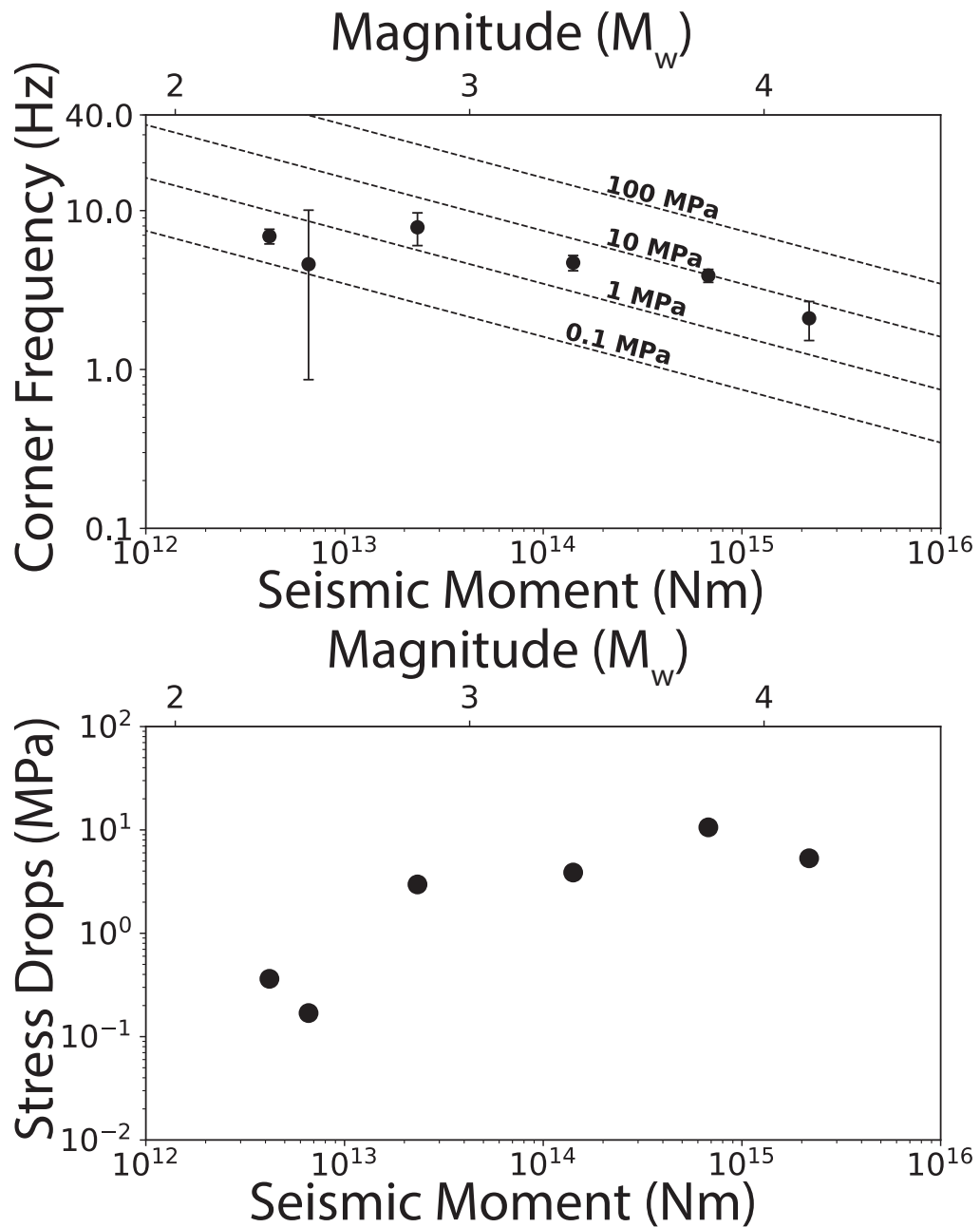
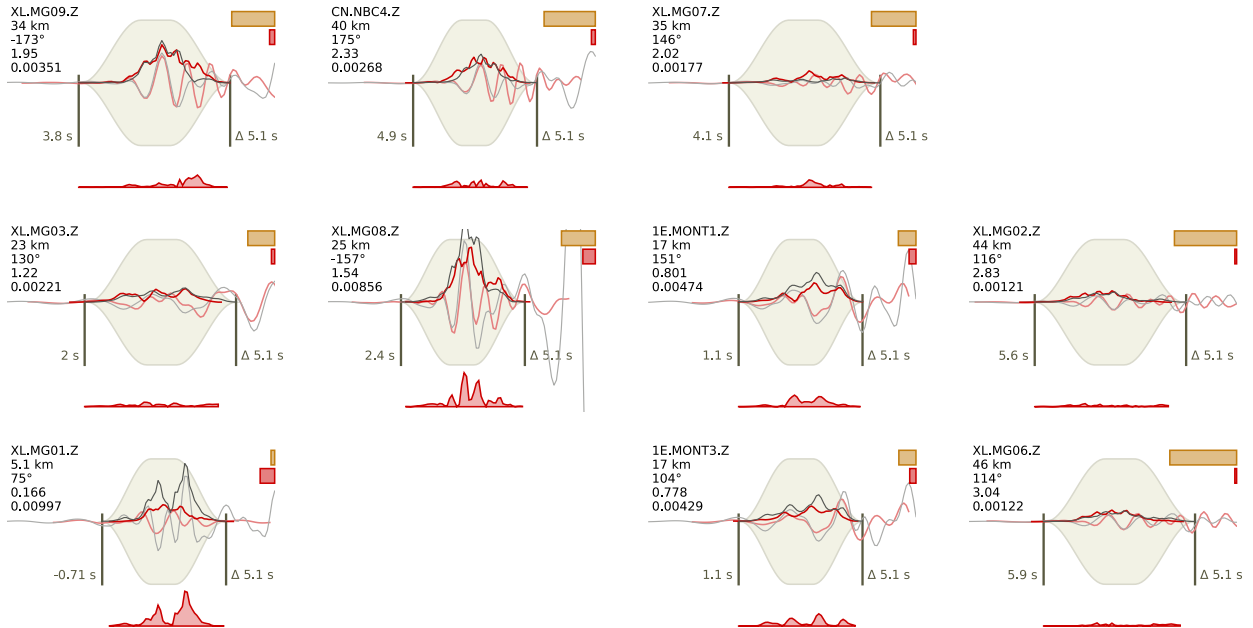
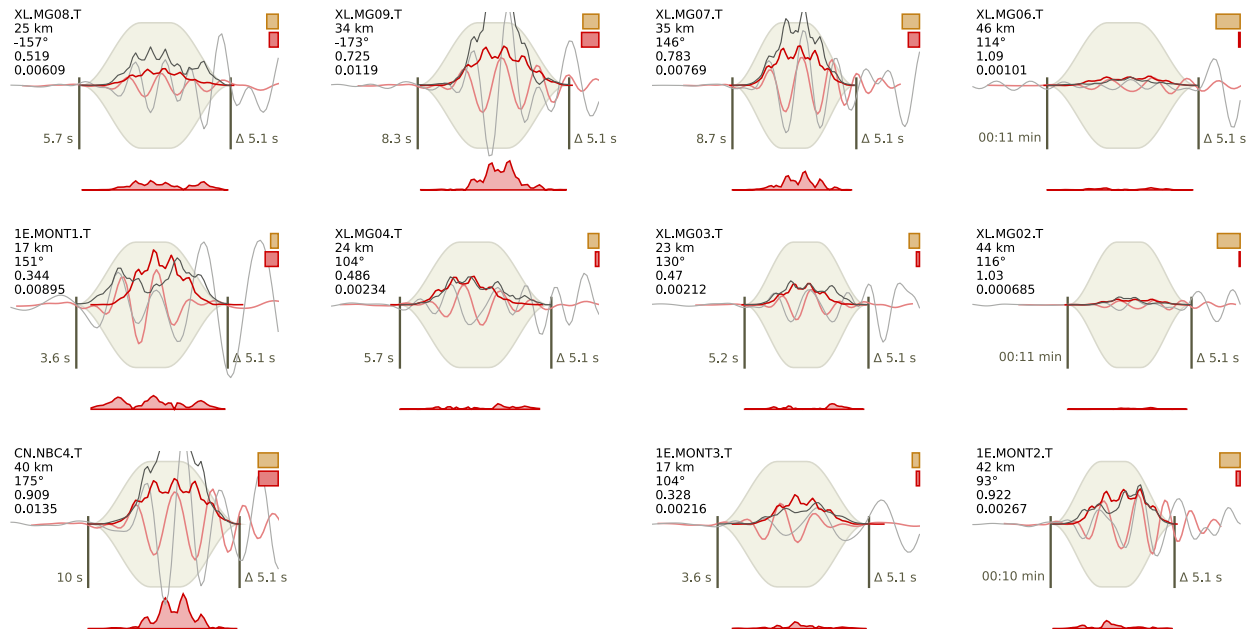


Figure S6. Corner frequency versus seismic moment. The black dots represent corner frequency estimates for one foreshock, the mainshock, and four aftershocks. Dashed lines show constant stress drop lines computed assuming a shear wave velocity of 3.3 km/s. Error bars indicate 95% confidence intervals of each event corner frequency estimate.

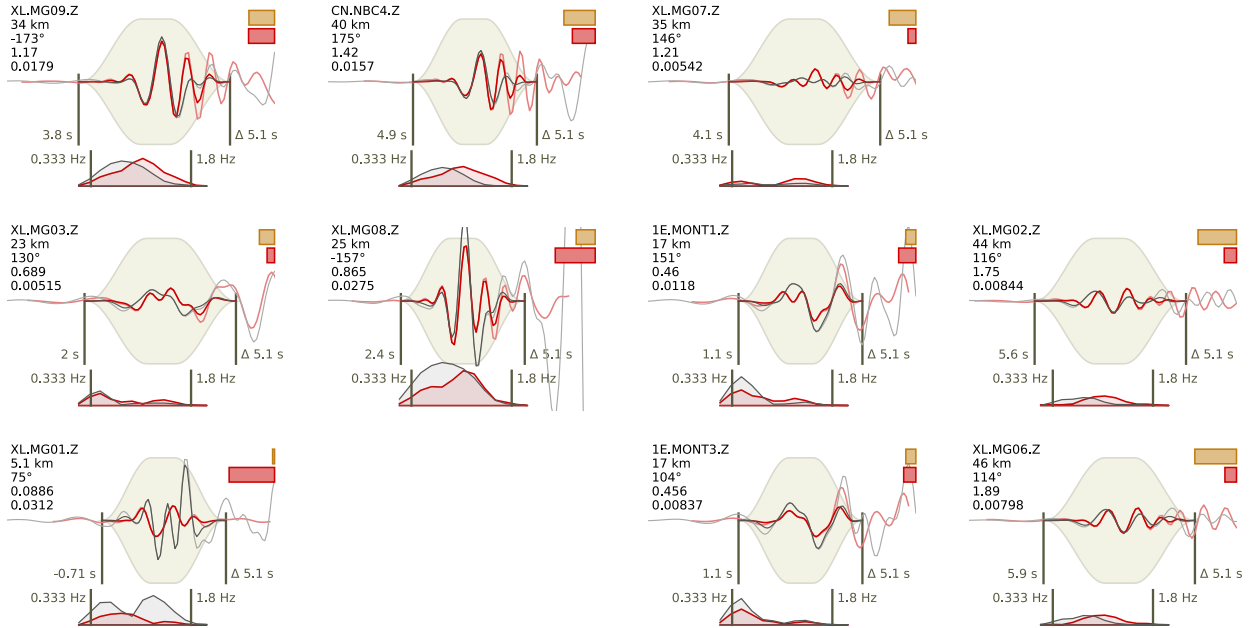
(a). Envelope domain (P waves)



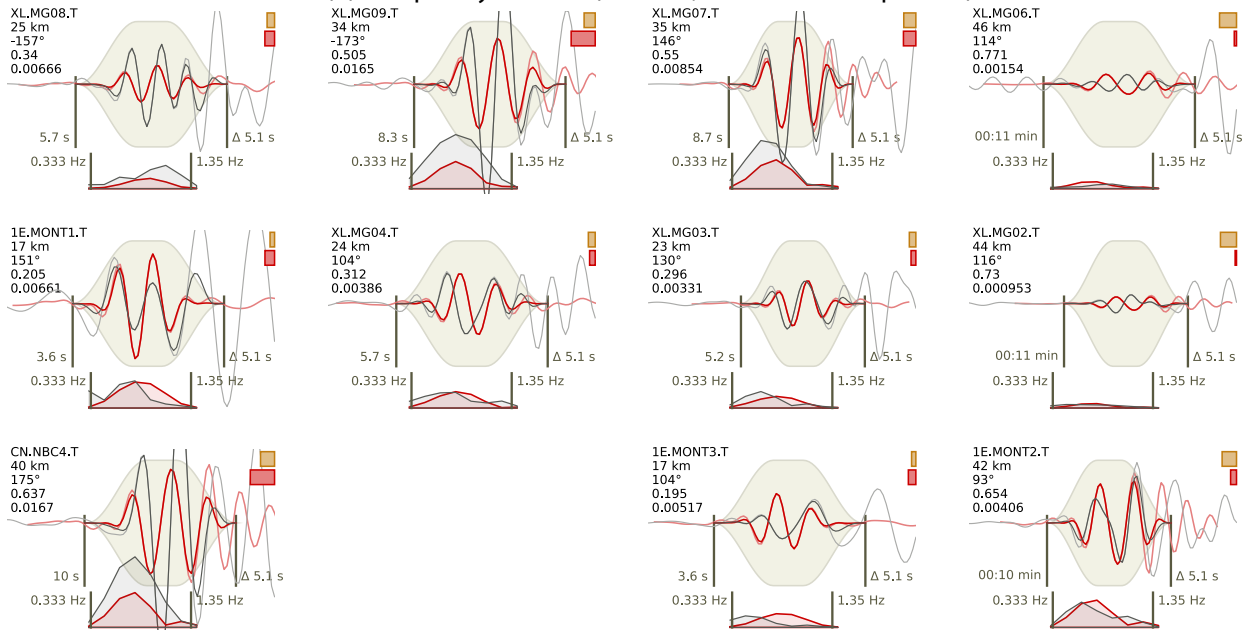
(b). Envelope domain (S waves, transverse component)



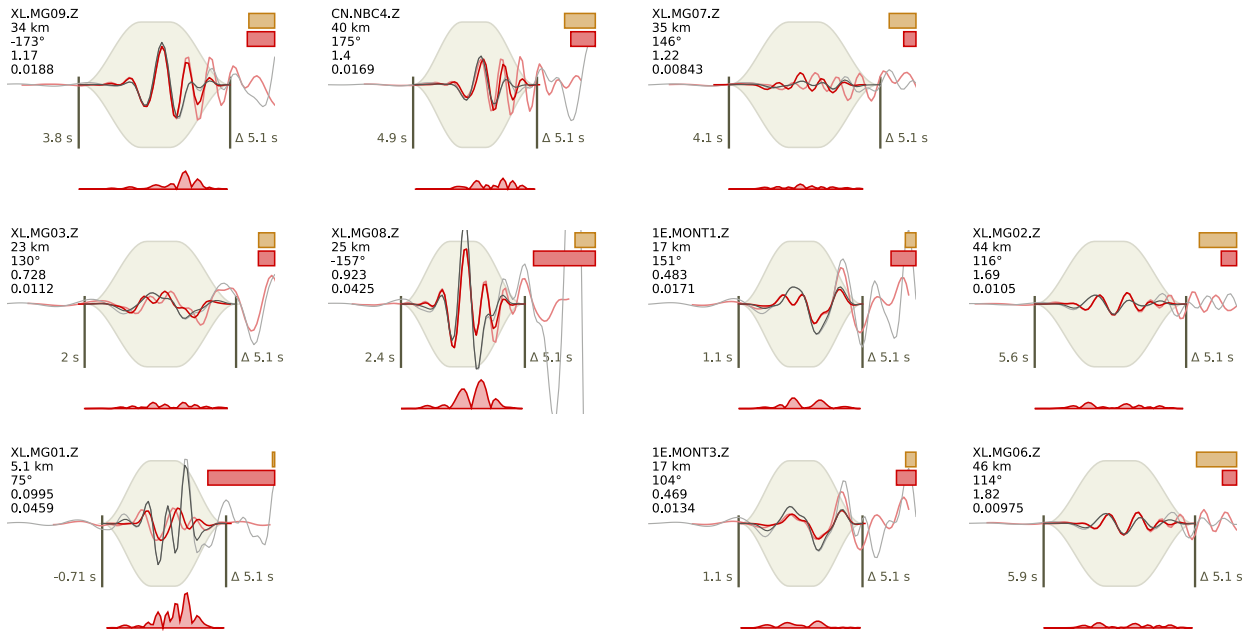
(c). Frequency domain (P waves)



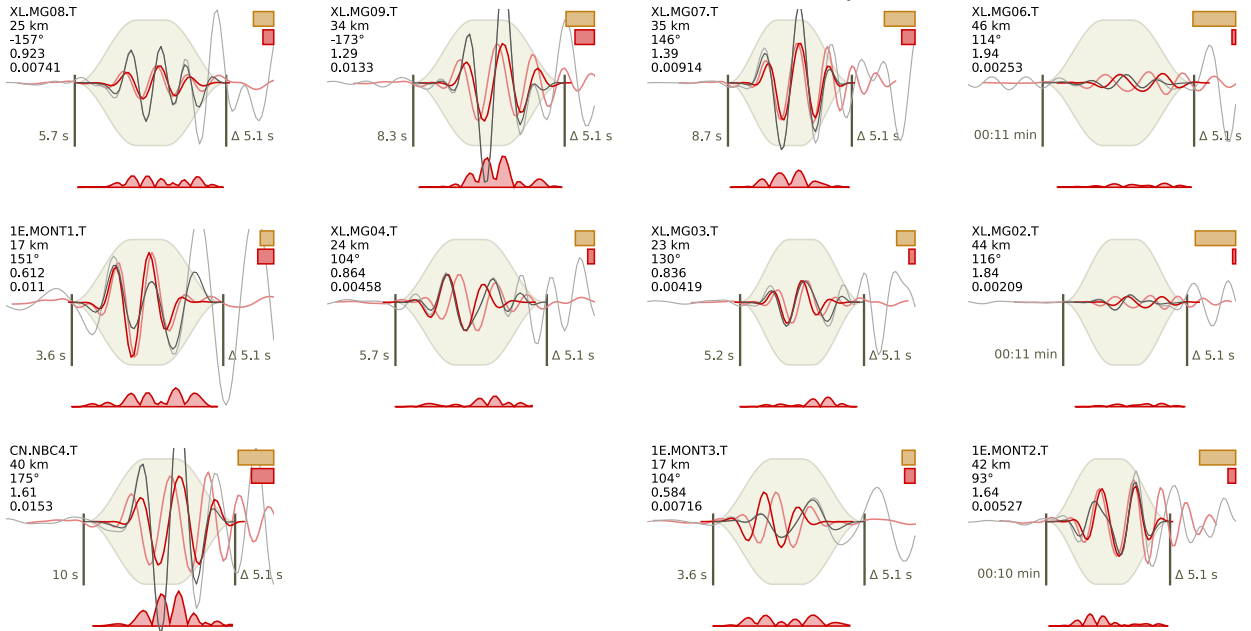
(d). Frequency domain (S waves, transverse component)



(e). Time domain (P waves)



(f). Time domain (S waves, transverse component)



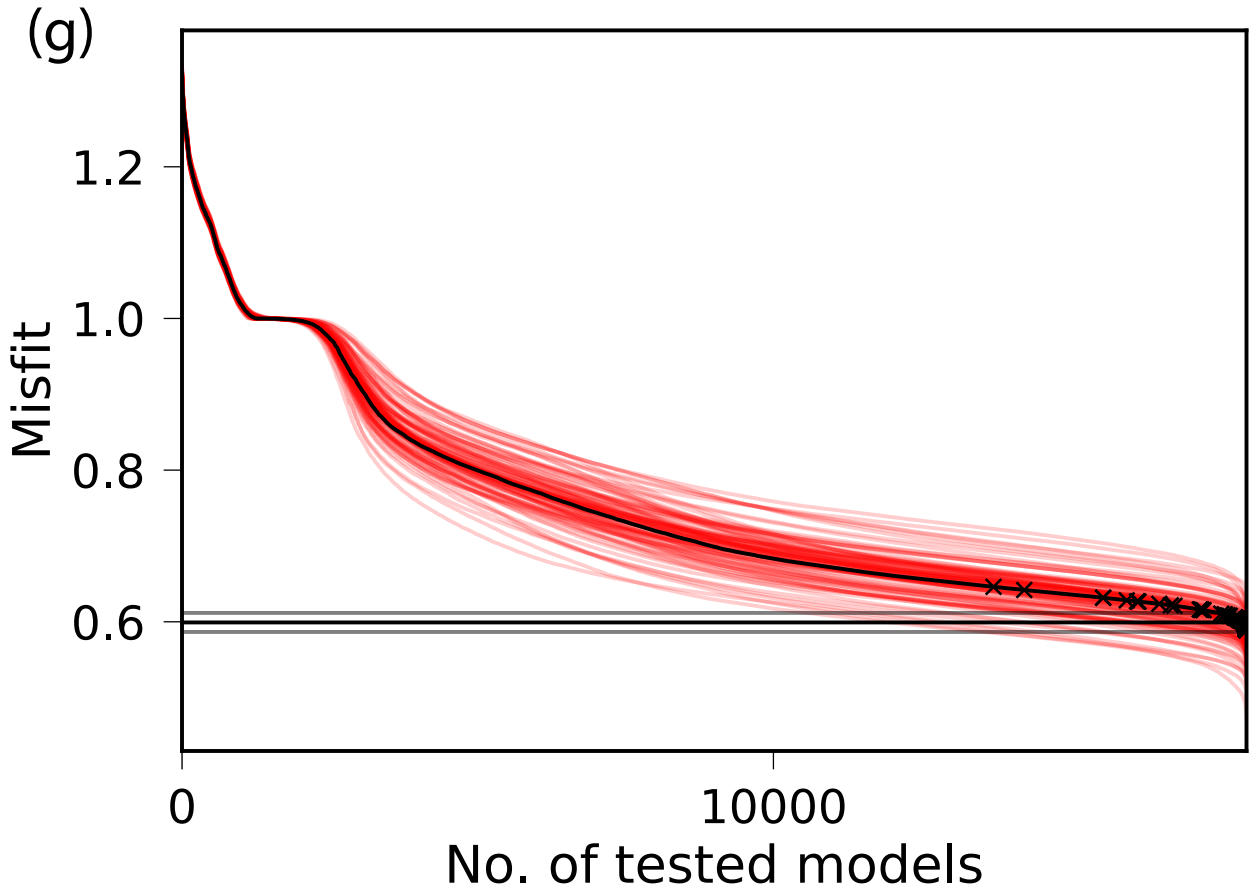


Figure S7. Waveform fitting for the M_L 4.5 mainshock for P-wave and S-wave in (a-b) envelope, (c-d) frequency domain, and (e-f) time domain. Black and red traces represent observed and synthetic waveforms respectively. Light and strong colors indicate tapered and untapered data, respectively. Light red traces are unshifted, dark red lines indicate the final fits. Residuals are given by the red trace at the bottom of each graph. Relative weighting factor (balancing weights during inversion) and relative residuals are indicated by yellow and red bars, respectively. Network, station, and component; station-epicenter distance; source-to-station azimuth; solution weight factor; and normalized residual are indicated to the right of each plot in (a-f). The value on the left-hand side (of each single panel showing an inversion) is the onset time with respect to the event origin; the time interval between the two black marker lines is indicated on the right. The global misfit is shown in (g). January 27, 2020, 3:34am

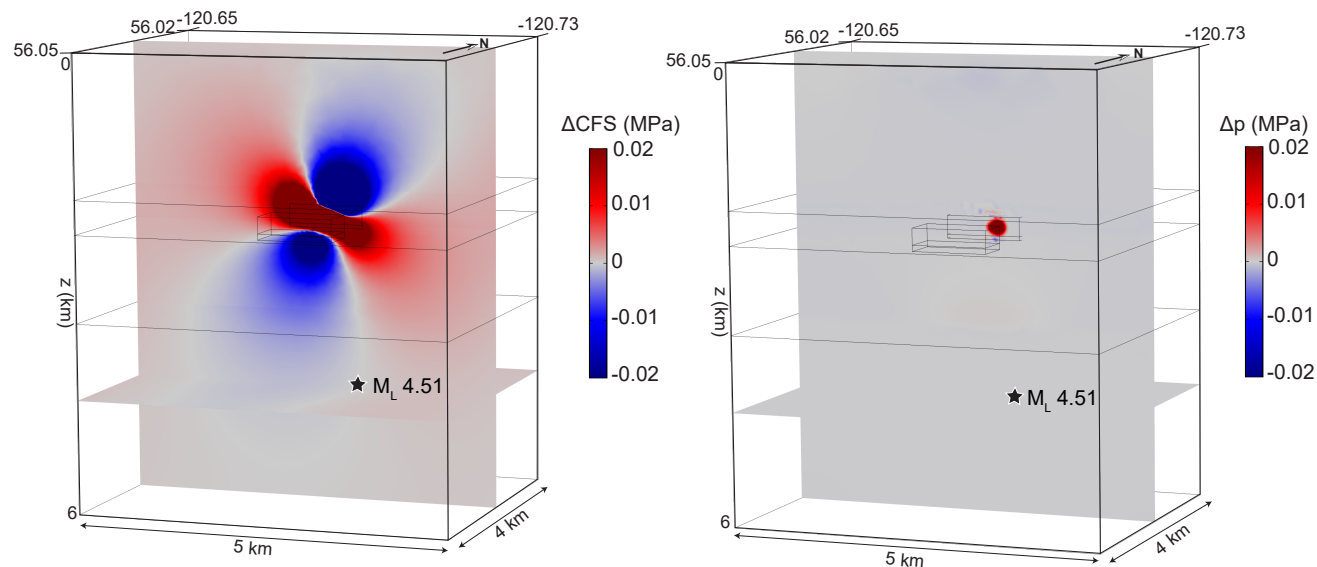


Figure S8. Coulomb stress (ΔCFS) (left) and pore pressure changes (Δp) (right) due to fluid injections calculated on the geometry and kinematics of the M_L 4.5 mainshock just before the occurrence of the earthquake using a poroelastic model without high-permeability fault zones. At the mainshock location, we calculate no pore pressure changes (right), and ΔCFS of 0.00015 MPa (left). Permeability values for the different layers are listed in Table 5

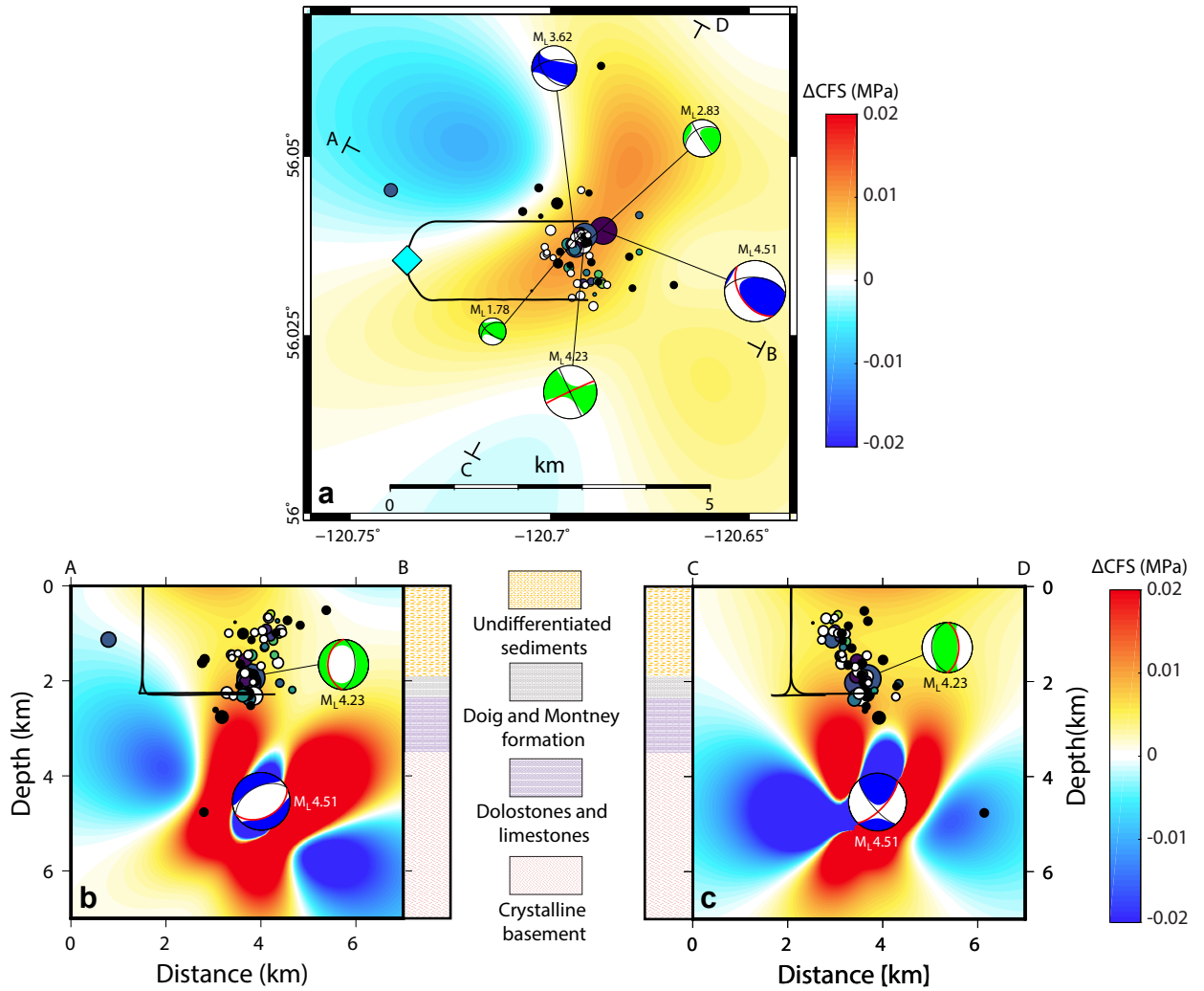


Figure S9. Coulomb stress changes (ΔCFS) calculated based on the geometry and kinematics of the M_L 4.2 aftershock (green focal mechanism, red line) inferred from the solution of the north-east dipping fault plane (blue focal mechanism, red line). ΔCFS are shown on (a) map view at 1.9 km calculation depth, and (b, c) on cross-section.

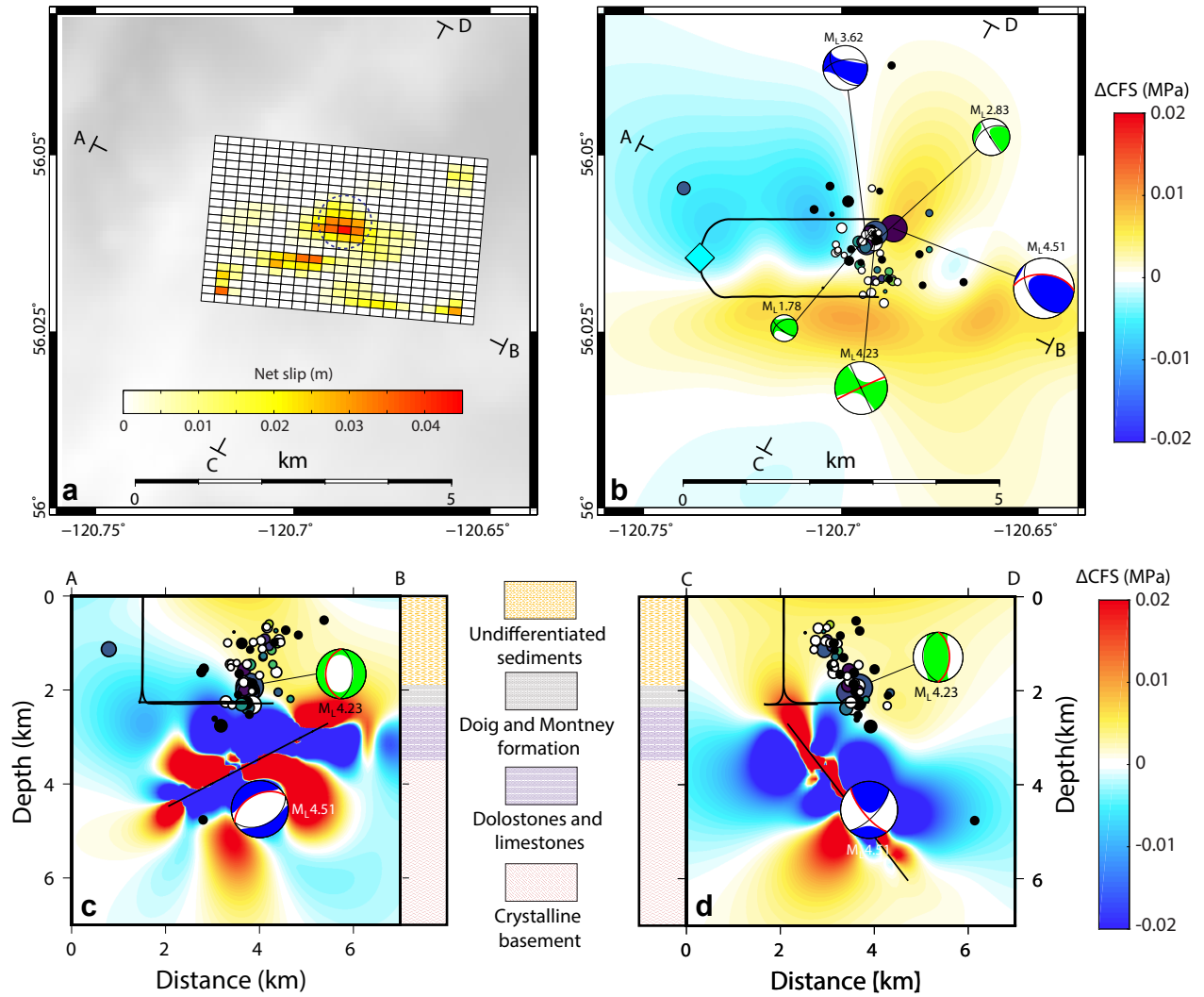


Figure S10. Coulomb stress changes (ΔCFS) calculated based on the geometry and kinematics of the $M_L 4.2$ aftershock (green focal mechanism, red line) inferred from the solution of the north-east dipping fault plane (blue focal mechanism, red line) calculated using a finite slip model based on full waveform inversion (a). ΔCFS is shown on (b) map view at 1.9 km calculation depth, and (c, d) on cross-section. The dashed circle in (a) represents the slip area adopted in the uniform slip model.

Tables

Depth to bottom of layer (km)	P-wave velocity (km/s)	S-wave velocity (km/s)
0.	2.5	1.07
1.	4.8	2.8
2.	5.5	3.2
4.	6.1	3.5
8.	6.2	3.6
25.	6.5	3.7
33.	8.045	4.48

Table S1. Velocity model used for *NonLinLoc* catalog location, *HypoDD* earthquake relative relocation calculation, and *Grond* Green’s function database calculation, adapted from Crust1.0 (Laske et al., 2013) (for layers above 1 km) and from (Mahani et al., 2017) (for deeper layers).

Name	Date, Origin Time	Magnitude	# of Channels	# of Detections
Mainshock	11/30/2018, 01:27:05	4.5	45	30
Template 1	05/05/2018, 14:39:03	2.8	27	18
Template 2	11/30/2018, 01:34:41	1.5	20	21
Template 3	11/30/2018, 02:06:01	3.6	45	47
Template 4	11/30/2018, 02:15:00	4.2	45	54
Template 5	11/30/2018, 10:36:58	1.3	29	107
Template 6	11/30/2018, 11:30:27	2.0	39	16
Template 7	12/02/2018, 23:24:40	1.2	18	8

Table S2. Template earthquakes used in the Multi-station Matched Filter (MMF) enhanced catalog detection in the 20 days surrounding the M_L 4.5 mainshock. Events consist of the mainshock and six well-recorded aftershocks, as well as a well-recorded event located on a fault structure antithetic to the M_L 4.5 event.)

Event Origin time	Seismic moment (Nm)	Moment magnitude	Corner freq. (Hz)	Confidence intervals (Hz)	Stress drop (MPa)
2018-11-29T11:44:29	6.591295e+12	2.5	4.6	-3.74/+5.46	0.17
2018-11-30T01:27:07	2.178520e+15	4.2	2.1	-0.58/+0.58	5.32
2018-11-30T02:06:02	1.414627e+14	3.4	4.7	-0.52/+0.52	3.87
2018-11-30T02:15:01	6.774354e+14	3.8	3.9	-0.37/+0.37	10.6
2018-11-30T02:35:30	4.187790e+12	2.3	6.9	-0.73/+0.73	0.36
2018-12-07T13:49:26	2.328523e+13	2.8	7.85	-1.83/+1.83	2.97

Table S3. Source parameter estimation (corner frequency and stress drop values)

Origin Time	Lat(°)	Long(°)	Depth (km)	Strikes	Dips	Rakes
2018-11-30T01:26:36	56.0357	-120.7189	2.7	[125,236]	[71,43]	[129,28]
2018-11-30T01:27:07	56.0432	-120.7168	4.4	[274,144]	[52,49]	[54,127]
2018-11-30T02:06:02	56.0411	-120.6972	3.0	[261,140]	[59,49]	[49,138]
2018-11-30T02:15:01	56.0473	-120.6897	2.9	[245,155]	[88,89]	[0,178]
2018-12-07T13:49:26	56.0453	-120.6973	2.5	[241,148]	[47,86]	[6,136]

Table S4. Fault planes solution from the focal mechanism solutions.

Origin Time	ISO (%)	CLVD (%)	DC (%)
2018-11-30T01:26:36	0.18	0.15	0.66
2018-11-30T01:27:07	0.02	0.24	0.74
2018-11-30T02:06:02	0.08	0.66	0.26
2018-11-30T02:15:01	0.08	0.42	0.50
2018-12-07T13:49:26	0.11	0.03	0.86

Table S5. Isotropic (ISO), compensated-Linear vector dipole (CLVD) and double-couple (DC) component for each of the events that focal mechanism was obtained.

Layer	Thickness ^a (km)	V _p (m/s)	V _s (m/s)	Density ^b (kg/m ³)	Porosity	k (m ²)	α
Undifferentiated sediments	1.9	4800	2740	2500	0.1	10 ⁻¹⁶	0.6
Doig and Montney formation (shales)	0.45	4800	2740	2500	0.1	10 ⁻¹⁸	0.8
Dolostones and limestones	1.15	5500	3200	2500	0.1	10 ⁻¹⁷	0.5
Crystalline basement	2.5	6100	3500	2790	0.05	10 ⁻¹⁹	0.4

Table S6. Elastic and hydrological parameters used in the poroelastic stress model. ^aData from the BCOGC (*British Columbia Oil and Gas Commission. Last accessed 2019/09/30, 2019*).

^bData from Crust 1.0 (Laske et al., 2013)

Dynamic viscosity	0.28 × 10 ⁻³ Pa s
Density	1000 kg/m ³
Compressibility	4.6 × 10 ⁻¹⁰ Pa ⁻¹

Table S7. Properties of injected fluids used in the poroelastic stress model.

References

- Abercrombie, R. E. (1995). Earthquake source scaling relationships from -1 to 5 ml using seismograms recorded at 2.5-km depth. *Journal of Geophysical Research: Solid Earth*, *100*(B12), 24015–24036.
- Boatwright, J. (1978). Detailed spectral analysis of two small New York State earthquakes. *Bulletin of the Seismological Society of America*, *68*(4), 1117–1131.
- British Columbia Oil and Gas Commission. Last accessed 2019/09/30. (2019). Retrieved 2019-09-30, from <https://www.bcogc.ca/>
- Brune, J. N. (1970). Tectonic stress and the spectra of seismic shear waves from earthquakes. *Journal of Geophysical Research*, *75*(26), 4997–5009.
- Burridge, R., & Knopoff, L. (1964). Body force equivalents for seismic dislocations. *Bulletin of the Seismological Society of America*, *54*(6A), 1875–1888.
- Eshelby, J. D. (1957). The determination of the elastic field of an ellipsoidal inclusion, and related problems. *Proceedings of the Royal Society of London. Series A. Mathematical and Physical Sciences*, *241*(1226), 376–396.
- Heimann, S., Isken, M., Kühn, D., Sudhaus, H., Steinberg, A., Vasyura-Bathke, H., . . . Dahm, T. (2018). *Grond - A probabilistic earthquake source inversion framework*. Retrieved 2018-08-27, from <http://pyrocko.org/grond/docs/current/> doi: 10.5880/GFZ.2.1.2018.003
- Laske, G., Masters, G., Ma, Z., & Pasyanos, M. (2013). Update on crust1. 0—a 1-degree global model of earth’s crust. In *Geophys. res. abstr* (Vol. 15, p. 2658).
- Lomax, A., Virieux, J., Volant, P., & Berge-Thierry, C. (2000). Probabilistic earthquake location in 3D and layered models. In *Advances in seismic event location* (pp. 101–134). Springer.

- Madariaga, R. (1976). Dynamics of an expanding circular fault. *Bulletin of the Seismological Society of America*, 66(3), 639–666.
- Mahani, A. B., Schultz, R., Kao, H., Walker, D., Johnson, J., & Salas, C. (2017). Fluid injection and seismic activity in the Northern Montney Play, British Columbia, Canada, with special reference to the 17 August 2015 Mw 4.6 induced earthquake. *Bulletin of the Seismological Society of America*, 107(2), 542–552. doi: 10.1785/0120160175
- Natural Resources Canada Earthquakes Canada, GSC, Earthquake Search (On-line Bulletin)*. (n.d.).
- Prieto, G., Parker, R., Thomson, D., Vernon, F., & Graham, R. (2007). Reducing the bias of multitaper spectrum estimates. *Geophysical Journal International*, 171(3), 1269–1281.
- Prieto, G., Parker, R., & Vernon III, F. (2009). A Fortran 90 library for multitaper spectrum analysis. *Computers & Geosciences*, 35(8), 1701–1710.
- Trugman, D. T., & Shearer, P. M. (2017). Growclust: A hierarchical clustering algorithm for relative earthquake relocation, with application to the Spanish Springs and Sheldon, Nevada, earthquake sequences. *Seismological Research Letters*, 88(2A), 379–391.
- Waldhauser, F., & Ellsworth, W. L. (2000). A double-difference earthquake location algorithm: Method and application to the northern Hayward fault, California. *Bulletin of the Seismological Society of America*, 90(6), 1353–1368.
- Wang, R. (1999). A simple orthonormalization method for stable and efficient computation of green's functions. *Bulletin of the Seismological Society of America*, 89(3), 733–741.
- Wang, R., Heimann, S., Zhang, Y., Wang, H., & Dahm, T. (2017). Complete synthetic seismograms based on a spherical self-gravitating earth model with an atmosphere–ocean–mantle–

core structure. *Geophysical Journal International*, 210(3), 1739–1764.

Wang, R., & Kümpel, H.-J. (2003). Poroelasticity: Efficient modeling of strongly coupled, slow deformation processes in a multilayered half-space. *Geophysics*, 68(2), 705–717.

Zhang, Y., Feng, W., Chen, Y., Xu, L., Li, Z., & Forrest, D. (2012). The 2009 L'Aquila Mw 6.3 earthquake: A new technique to locate the hypocentre in the joint inversion of earthquake rupture process. *Geophysical Journal International*, 191(3), 1417–1426.